Article:
Wang, S., Zhu, Z. orcid.org/0000-0001-7175-3307, Pride, A. et al. (3 more authors) (2022) Comparison of different winding configurations for dual three-phase interior PM machines in electric vehicles. World Electric Vehicle Journal, 13 (3). 51.

https://doi.org/10.3390/wevj13030051

World Electric Vehicle Journal

MDPI

Article

Comparison of Different Winding Configurations for Dual Three-Phase Interior PM Machines in Electric Vehicles

Shensheng Wang [1], Ziqiang Zhu [1,*], Adam Pride [2], Juntao Shi [2], Rajesh Deodhar [2] and Chiaki Umemura [2]

[1] Department of Electronic and Electrical Engineering, University of Sheffield, Mappin Street, Sheffield S1 3JD, UK; swang104@sheffield.ac.uk
[2] IMRA Europe SAS UK Research Centre, Aisin Seiki Building, University of Sussex, Falmer, Brighton BN19RS, UK; ap@imra-ukrc.com (A.P.); jts@imra-ukrc.com (J.S.); rd@imra-ukrc.com (R.D.); cu@imra-ukrc.com (C.U.)
* Correspondence: z.q.zhu@sheffield.ac.uk

Abstract: In this paper, two dual three-phase winding configurations are compared based on the Toyota Prius 2010 interior permanent magnet (IPM) machine. It is found that the winding configuration with single-layer full-pitched (SF) windings can improve average torque and reduce torque ripple in constant torque range. The winding configuration with double-layer short-pitched (DS) windings has better torque performance in a constant power range. The electromagnetic performances of the two winding configurations when one winding set is excited and the other one is open-circuited are also compared. The DS winding configuration shows much better performance under this condition. Overall, the dual three-phase winding configuration with DS windings is preferred for dual three-phase IPM machines in electric vehicles. A Toyota Prius 2010 IPM machine equipped with DS windings was manufactured to verify the analyses presented in this paper.

Keywords: dual three-phase; interior permanent magnet; IPM machine; winding configuration

Citation: Wang, S.; Zhu, Z.; Pride, A.; Shi, J.; Deodhar, R.; Umemura, C. Comparison of Different Winding Configurations for Dual Three-Phase Interior PM Machines in Electric Vehicles. *World Electr. Veh. J.* **2022**, *13*, 51. https://doi.org/10.3390/wevj13030051

Academic Editor: Joeri Van Mierlo

Received: 16 February 2022
Accepted: 8 March 2022
Published: 11 March 2022

1. Introduction

In recent decades, electric vehicles (EVs) have attracted more and more attention with the concerns about global greenhouse gas emissions and the unstable supplies of fossil fuels. Since electrical machines are one of the most important components in the propulsion system in EVs, developing a high-performance machine specialized for EVs can greatly improve the overall performance of the vehicles. Among different kinds of machines, interior permanent magnet (interior PM, IPM) synchronous machine (SM) is regarded as a suitable choice for EV machines, as it has inherent high torque capacity, high torque density, and high efficiency [1–5].

To further improve the performance of PMSMs, the dual three-phase (DTP) winding configuration is introduced, and some research has been conducted based on DTP PMSMs [6–35]. Compared with conventional single three-phase (STP) machines, the advantages of DTP PMSMs include:

- Higher torque. The winding factors of the original windings can be improved by the DTP winding configuration [6,23];
- Lower torque ripple. The specific torque harmonics produced by the two winding sets can be cancelled with each other, and the stator magnetomotive force (MMF) harmonics are significantly reduced by DTP windings [9,14,22];
- Higher efficiency. Due to the reduced stator MMF harmonic contents of DTP windings, the PM eddy losses in the DTP machines are lower than those in the STP counterpart. Considering that DTP windings can improve the output torque/power, the efficiency can be increased by the DTP winding configuration [11];

- Better fault-tolerant capacity. There are two separate winding sets in DTP windings, and hence, the loss of one winding set will not lead to the failure of the whole system. The DTP machine can be operated with the remaining healthy winding set [8,17–19].

Besides the advantages listed above, the ratings per phase are reduced with the increase in phase number. The vibration of PWM frequency can also be reduced by two parallel inverters in a DTP machine [31–34]. Moreover, the two winding sets provide more control freedoms in a machine system, and thus, more control strategies can be utilized, and the performance of DTP machines can be further improved [35].

However, most of the existing literature only focuses on fractional-slot PMSM, not the most widely employed machines in EVs, i.e., integral-slot PMSMs. Since fractional-slot PMSMs and integral-slot PMSMs have different slot/pole number combinations, their winding layouts are also different. The coil pitch number in fractional-slot PMSMs is usually relatively small. When the coil pitch number equals 1, the windings can also be called tooth coils or non-overlapping concentrated windings. For integral-slot PMSMs, the coil pitch number is around the number of slots per pole. These windings are called overlapping distributed windings. Considering the differences in slot/pole number combinations and winding configurations between fractional-slot PMSMs and integral-slot PMSMs, the conclusion obtained from fractional-slot PMSMs may not be used in integral-slot PMSMs directly. Thus, it is still meaningful to analyze the electromagnetic performance of integral-slot DTP PMSMs and compare it with that of the STP counterpart.

In this paper, the Toyota Prius 2010 IPM machine, which is a 48-slot/8-pole IPMSM, is chosen as the benchmark. For the 48 slot/8-pole IPMSM, two DTP winding configurations have been proposed in existing literature [13,36–38]. The DTP winding configuration with single-layer full-pitch windings (DTP-SF) was introduced in [36,37]. However, the differences between the original short-pitched windings and the proposed full-pitched windings are not considered thoughtfully. The DTP winding configuration with double-layer short-pitched windings (DTP-DS) can be found in [13,38]. However, the electromagnetic performance of DTP-DS has not been presented comprehensively in existing papers, and the proposed DTP-DS winding configuration has never been compared with the conventional STP winding configuration in the Toyota Prius 2010 IPM machine. In this paper, the two DTP winding configurations are compared with each other for the first time, and both of them are compared with the original winding configuration. The comparisons are made using the finite element (FE) method over the whole speed range because the electromagnetic characteristics of the IPMSMs with these winding configurations can be affected obviously by rotation speed. Furthermore, for DTP-SF and DTP-DS machines, even if one three-phase winding set is open-circuited (OC), they still can be operated with the remaining three-phase winding set. To compare their electromagnetic performances under this condition, the comparison carried out under the three-phase OC condition is also considered. From the comparative studies given in this paper, the DTP-DS winding configuration is preferred for the Toyota Prius 2010 IPM machine.

This paper is structured as follows: the details of different winding configurations are provided in Section 2. In Section 3, the electromagnetic performances of these winding configurations are compared under healthy conditions in various aspects, including output torque capacity, torque ripple, torque-speed characteristic, efficiency, and so on. In Section 4, the electromagnetic performances of two DTP winding configurations are compared under three-phase OC conditions in similar aspects. The experimental verification is given in Section 5, followed by the conclusion in Section 6.

2. Winding Configurations

The Toyota Prius 2010 IPM machine is well known for its excellent performance and has been investigated by researchers all over the world in recent years [39–41]. The cross-section of the machine with a 48-slot stator and an 8-pole V-type IPM rotor is presented in Figure 1.

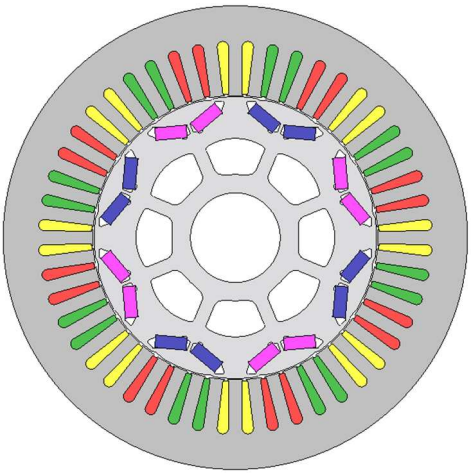

Figure 1. Cross-section of the Toyota Prius 2010 machine.

The main design specifications of the machine can be found in [41], as shown in Table 1.

Table 1. Design specifications of Toyota Prius 2010 IPM machine.

Number of Stator Slots	48	Number of Rotor Poles	8
Stator OD, mm	264	Rotor OD, mm	160.44
Stator ID, mm	161.9	Rotor lamination ID, mm	51
Stator stack length, mm	50.8	Lamination thickness, mm	0.305
Slot depth, mm	30.9	Slot opening, mm	1.88
Phase resistance, Ohm	0.077	Magnet dimensions, mm	49.3 × 17.88 × 7.16

The detailed characteristics of the magnets in the machine are investigated and provided in [41]. The intrinsic hysteresis graphs of the magnets are plotted in [41], considering different temperatures. The diminishing nature of the remanent flux density and coercivity with increasing temperature can be observed. However, in this paper, the simulations are calculated using JMAG-Designer, which is a simulation software for the development and design of electrical devices provided by JSOL [42]. To simplify the calculation in simulations, the ideal permanent magnet material 'NdFeB_Br = 1.2T' is chosen as the magnets in the JMAG model, and B_r and μ_r of 'NdFeB_Br = 1.2T' are fixed at 1.2T and 1.05, respectively. Further, in the JMAG model, '35H270' is chosen as the stator and rotor core materials, and the calculated iron losses in this paper are based on the properties of '35H270' in JMAG software.

2.1. Winding Arrangements

The stator windings equipped in the Toyota Prius 2010 PM machine are 5-slot-pitched single layer three-phase windings, as shown in Figure 2a. In 48-slot/8-pole IPM machines, the number of slots per pole is 6. Hence, the original windings in the Toyota Prius 2010 IPM machine are short-pitched windings, which can reduce MMF harmonics and end-winding length. The diagram of coil electromotive force (EMF) phasors is given in Figure 2b. It can be seen that there is no phase shift between the coil EMF phasors of the same phase. In other words, the original three-phase windings cannot be transferred into two three-phase windings with a 30° phase shift.

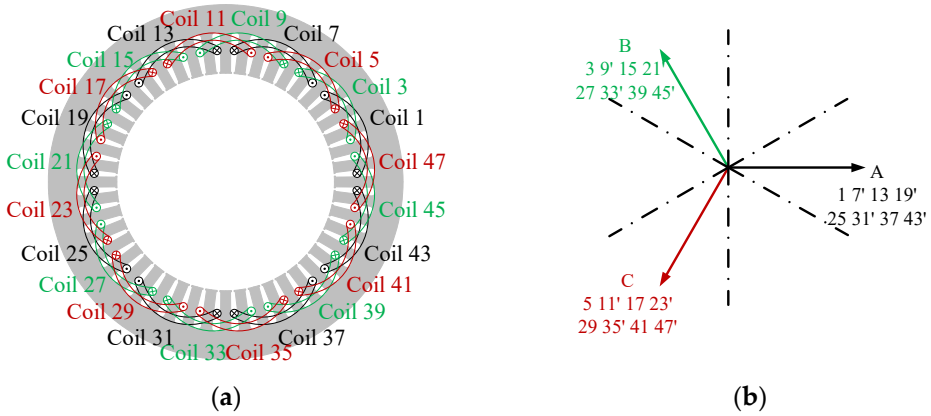

Figure 2. Winding arrangements of Toyota Prius 2010 IPM machine: (**a**) winding layouts; (**b**) coil EMF phasor diagram.

As is well-known in existing literature [6], the DTP winding configuration with a 30° phase shift can improve output torque and reduce torque harmonics at the same time in PMSMs. To realize the advantages of the 30° DTP configuration in 48-slot/8-pole IPMSMs, two DTP winding configurations have been proposed. Different from the original single-layer short-pitched windings, the stator windings utilized in the two DTP winding configurations are single-layer full-pitched (SF) windings and double-layer short-pitched (DS) windings, respectively. In this paper, the three different winding configurations are designated as the original IPMSM (ORG), DTP-SF, and DTP-DS, respectively. The winding connections of Phase A in the ORG machine and those of Phases A1 and A2 in the DTP-SF and DTP-DS machines are shown in Figure 3.

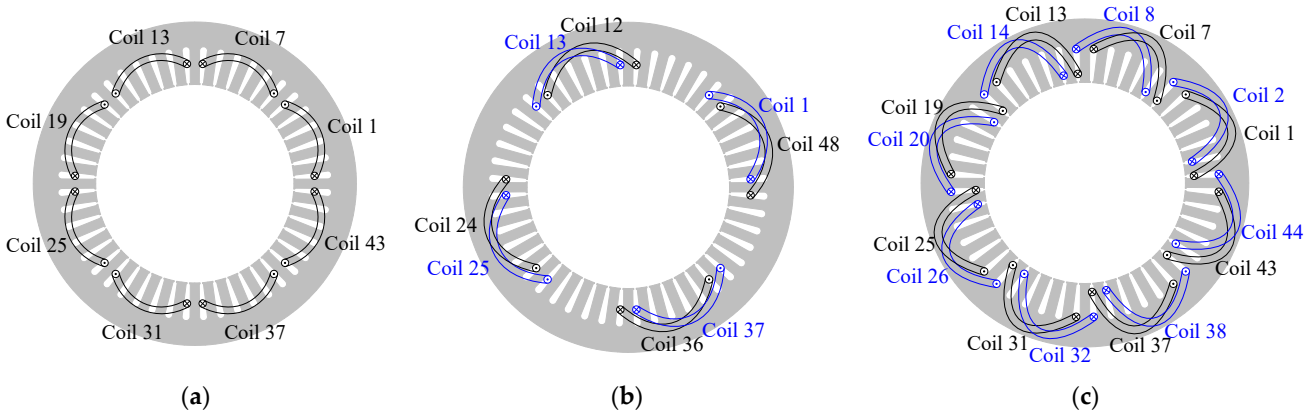

Figure 3. Winding layouts of Phase A in ORG machine and Phases A1 and A2 in DTP machines: (**a**) ORG; (**b**) DTP-SF; (**c**) DTP-DS.

In the ORG machine, as shown in Figure 3a, the coils of Phase A are Coils 1, 7, 13, 19, 25, 31, 37, and 43. The interval between adjacent coils is 8 slot pitches in space, which is 180° in electrical degree. Compared with Coils 1, 13, 25, and 37, Coils 7, 19, 31, and 43 are opposite connected. Thus, all the coils of Phase A in the ORG machine share the same back EMF phases, as shown in Figure 2b. In the DTP-SF machine, the coil pitch number is 6 slot pitches instead of 5 slot pitches in ORG and DTP-DS machines. The detailed winding layouts of the DTP-SF winding configuration are shown in Figure 3b. It can be seen that the distance between Coil 1 and Coil 48 is one slot pitch in space, which is 30° electrical degrees. In other words, the back EMFs induced in Coil 48 are ahead of that in Coil 1 by 30°. Similarly, the back EMFs induced in Coils 12, 24, and 36 are advanced to those in Coils 13, 25, and 37 by 30°. In DTP-SF windings, Phase A1 is composed of Coils 48, 12, 24, and 36, and Phase A2 is composed of Coils 1, 13, 25, and 37. Thus, Phase A1 is ahead of

Phase A2 by 30°. In the DTP-DS machine, the original windings are duplicated, and the new winding set is shifted by one slot pitch, as shown in Figure 3c. The coils of Phase A in the ORG machine, Coils 1, 7, 13, 19, 25, 31, 37, and 43, belong to Phase A1 in the DTP-DS machine, and the new Coils 2, 8, 14, 20, 26, 32, 38, and 44 belong to Phase A2. Thus, all the coils of Phase A2 lag behind those of Phase A1 by one slot pitch, which means that the back EMF of Phase A2 is lag to that of Phase A1 by 30° in time. Overall, the resultant stator winding arrangements of ORG, DTP-SF, and DTP-DS winding configurations are shown in Figure 4a–c. The coil EMF phasor diagrams of these winding configurations are shown in Figure 5a–c.

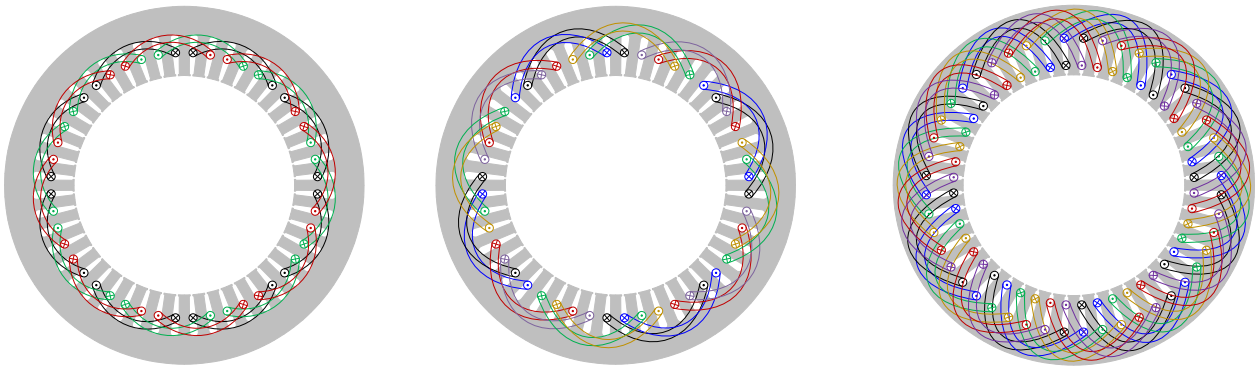

(**a**) (**b**) (**c**)

Figure 4. Winding arrangements of different winding configurations: (**a**) ORG; (**b**) DTP-SF; (**c**) DTP-DS.

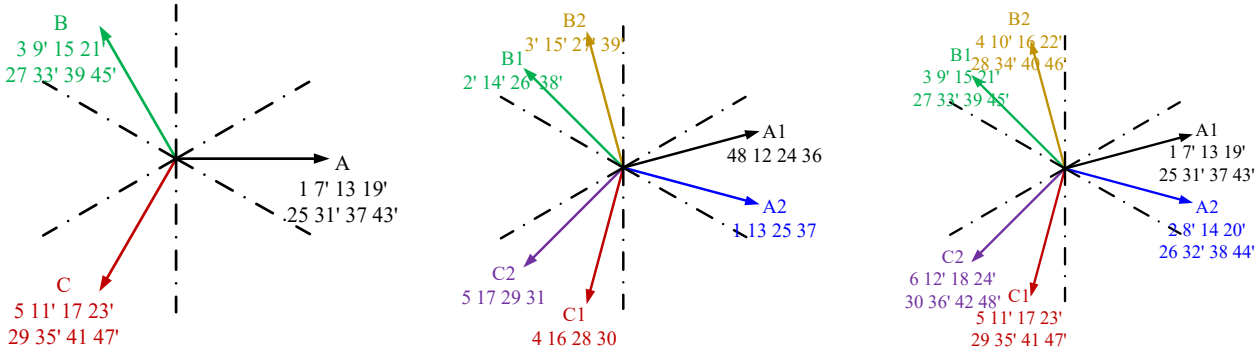

(**a**) (**b**) (**c**)

Figure 5. Coil EMF phasor diagrams of different winding configurations: (**a**) ORG; (**b**) DTP-SF; (**c**) DTP-DS.

2.2. Winding Specifications

Besides the difference in winding arrangements, the drive system for DTP-SF and DTP-DS winding configurations is also different from the original one, as shown in Figure 6a,b. The original inverter is a three-phase six-switch voltage source inverter (VSI), and the DC-link voltage is rated at 650 Vdc. DTP machines are fed by two separate three-phase inverters, and the two inverters are parallel connected. Compared with the ORG machine, the input power of DTP machines is split into two winding sets. Considering that the two winding sets in DTP machines share the same DC-link voltage with the original windings, the phase currents in DTP windings can be halved from the original phase currents in ORG windings to produce equivalent power. In the ORG machine, the maximum torque is produced with 236 Apk peak phase currents. Compared with the original machine, the number of turns is doubled in DTP machines, and thus, phase currents should be halved to keep the same equivalent ampere-turns. In other words, to make the comparison

fair, 118 Apk peak phase currents are utilized in DTP machines to produce the largest torque. Hence, the current requirement for DTP inverters can also be halved from the original value in the ORG machine. The lower current requirement suggests that cheaper power devices can be utilized in DTP inverters. Although the number of switches is doubled in the DTP drive system, the total cost of the DTP drive system is lower than twice the original cost. For example, according to the 'IGBT Module Finder' tool provided by Infineon Technologies [43], FS400R07A1E3 can be chosen for the ORG drive system, and FS200R07A1E3 can be chosen for DTP-SF and DTP-DS drive systems. Since both FS400R07A1E3 and FS200R07A1E3 are three-phase six-pack modules, only one module is needed in the ORG machine, and two modules are required in DTP machines. As ORG and DTP machines share the same DC-link properties, the difference in the prices of semiconductor modules is the only difference in the resulting cost of different drive systems.

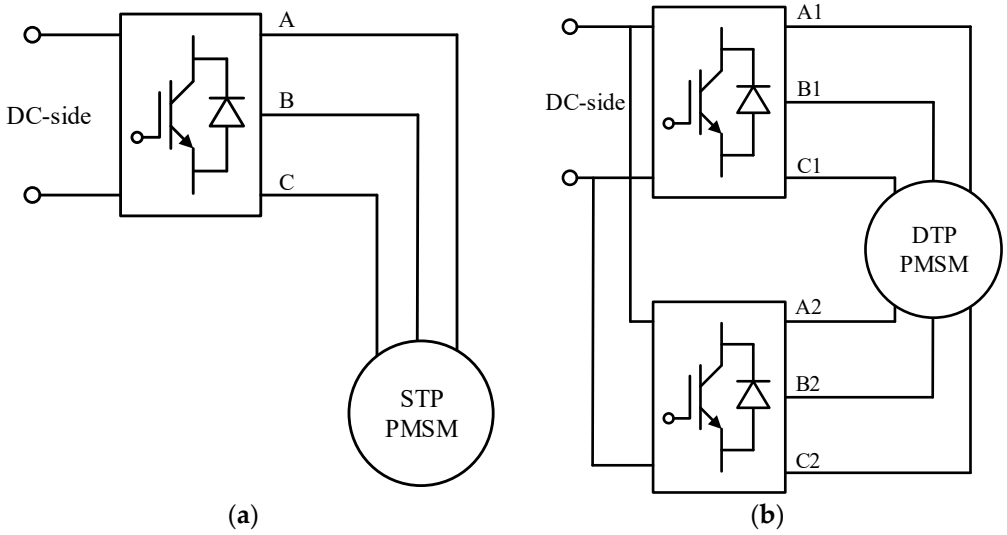

Figure 6. Schematics of drive systems for different winding configurations: (**a**) ORG; (**b**) DTP-SF; DTP-DS.

The detailed parameters of different winding configurations are summarized in Table 2. As shown in Figure 3, the number of coils in series per phase is eight in ORG and DTP-DS machines and four in the DTP-SF machine. As mentioned before, the current requirement is halved in DTP windings. Thus, the number of wires per turn in parallel can also be halved from 12 in ORG windings to 6 in DTP-SF and DTP-DS windings. However, it should be mentioned that the number of turns per coil in DTP-SF windings needs to be doubled from 11 to 22 after the currents are halved because the number of turns per slot should be doubled to keep the total ampere-turns the same after the change. The number of turns per coil does not need to be changed in the DTP-DS machine because the number of turns per slot is doubled by using double-layer winding layouts. Another difference between different winding configurations is the coil pitch number, which is 5 in ORG and DTP-DS machines and 6 in DTP-SF machines. Assuming the end-windings are semi-circular in shape, the schematics of each turn in different windings are also plotted in Table 2.

As shown in Table 2, the windings utilized in different winding configurations are quite different. The phase resistances of DTP-SF and DTP-DS windings should be re-calculated according to the phase resistance of ORG windings. It is known that the resistance of a conductor can be computed as

$$R = \rho \frac{l}{A} \tag{1}$$

where l is the length of the conductor, A is the cross-sectional area of the conductor, and ρ is the electrical resistivity of the conductor. To obtain the phase resistance of DTP-SF and

DTP-DS windings, the relationships of total winding length and cross-sectional area of DTP-SF and DTP-DS windings to those of ORG windings should be obtained firstly.

Table 2. Specifications of different winding configurations.

	ORG	DTP-SF	DTP-DS
Number of phases	3	6	6
Coils in series per phase	8	4	8
Turns in series per coil	11	22	11
Wires in parallel per turn	12	6	6
Coil pitch number	5	6	5
Parallel circuits per phase	0	0	0
Wire diameter, mm	0.8	0.8	0.8
Schematic of each turn	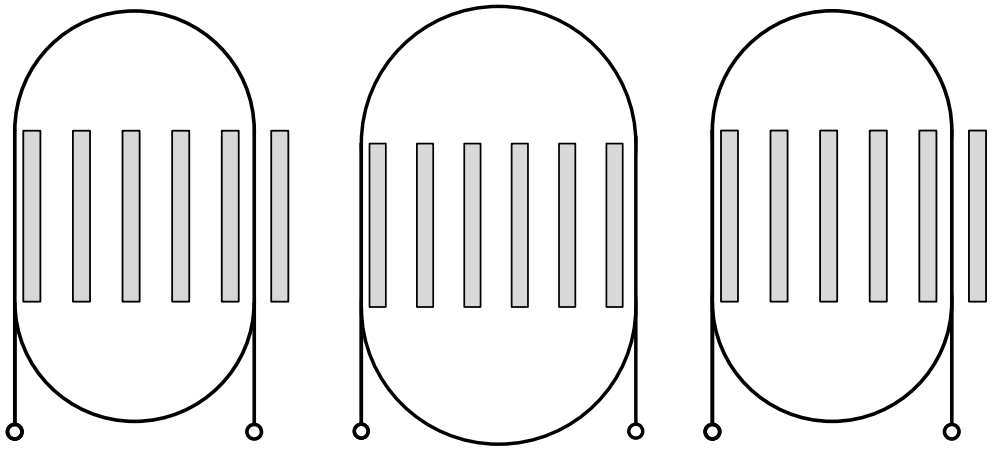		

The cross-sectional area of these windings can be easily obtained. From Table 2, it is known that there are no parallel circuits in these windings, and the same copper wires are utilized in three windings. The cross-sectional area of each coil is the product of the number of wires per coil and the cross-sectional area of each wire. From Table 2, there are 12 strands of wires in ORG windings, and only 6 strands of wires in DTP-SF and DTP-DS windings. Thus, the cross-sectional area of DTP-SF and DTP-DS windings is half of that of ORG windings.

However, the total winding length is relatively difficult to compute directly because the lengths of different coils are different according to the position of their two sides in the slot. In this paper, to simplify the calculation, all coil sides are assumed at the center of slots. Thus, the total winding length can be estimated from the total number of turns in series per phase and the length of each turn. The number of coils per phase and the number of turns per coil are provided in Table 2. It can be found that the three winding configurations share the same number of turns in series per phase, which is 88. Thus, the resultant total winding length is proportional to the length of each turn.

From Figure 3 and Table 2, it can be seen that only the coil pitch number can affect the length of each turn under these assumptions. Since both the coil pitch numbers of ORG and DTP-DS windings are 5, the total winding lengths of the two winding configurations are identical. Considering that the cross-sectional area of DTP-DS windings is half compared with ORG windings, the phase resistance of DTP-DS windings is doubled from 0.077 Ohm in ORG windings to 0.154 Ohm.

For DTP-SF winding configuration, the coil pitch number is 6 and the full-pitched windings are utilized. To calculate the phase resistance of DTP-SF windings, the total lengths of short-pitched and full-pitched windings should be obtained first. As different windings share the same number of turns per phase, the lengths of different windings can be obtained from the length of short-pitched and full-pitched coils. The schematics of short-pitched and full-pitched coils are shown in Figure 7.

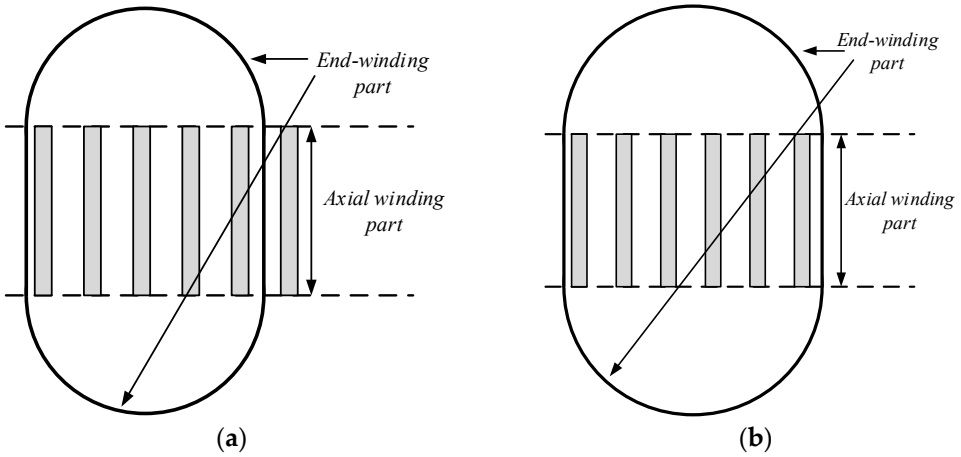

Figure 7. Schemes of different coils: (**a**) short-pitched coil; (**b**) full-pitched coil.

It can be seen that both coils can be divided into two parts: the axial winding part and the end-winding part. The length of the axial winding part is the stator's axial length. The length of the end-winding part can be calculated based on the stator's inner diameter, slot depth, and coil pitch number, and these data be found in Table 1. Since all coil sides are assumed to be at the center of slots, the equivalent radius of each coil side, r_e, is the sum of the stator's inner radius and a half of the slot depth, as shown in Figure 8.

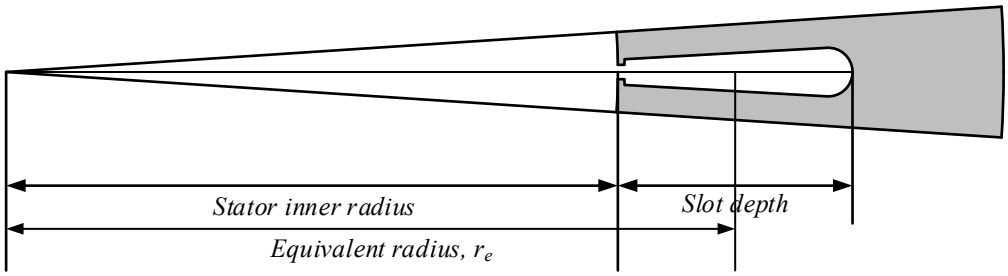

Figure 8. Schematic of the equivalent radius of the coil side.

Thus, the equivalent radius of each coil side, r_e, is

$$r_e = \frac{50.8}{2} + \frac{39.6}{2} = 96.4 \text{ mm} \tag{2}$$

Then, the distance between two coil sides in short-pitched coil, $l_{cs\text{-}s}$, and that in full-pitched coil, $l_{cs\text{-}f}$, can be obtained by taking the coil pitch number into consideration,

$$l_{cs\text{-}s} = 5\frac{2\pi r_e}{48} \approx 63.10 \text{ mm} \tag{3}$$

$$l_{cs\text{-}f} = 6\frac{2\pi r_e}{48} \approx 75.71 \text{ mm} \tag{4}$$

As shown in Figure 7, the distance between two coil sides is the diameter of the end-winding part. The length of each end-winding part in short-pitched coil, $l_{ew\text{-}s}$, and that in full-pitched coil, $l_{ew\text{-}f}$, can be calculated as

$$l_{ew\text{-}s} = \pi\frac{l_{cs\text{-}s}}{2} \approx 99.11 \text{ mm} \tag{5}$$

$$l_{ew\text{-}f} = \pi\frac{l_{cs\text{-}f}}{2} \approx 118.93 \text{ mm} \tag{6}$$

Assuming the stator axial length is l_a, the total length of short-pitched coil, l_s, and that of full-pitched coil, l_f, can be obtained as

$$l_s = 2l_a + 2l_{ew\text{-}s} = 299.82 \text{ mm} \quad (7)$$

$$l_f = 2l_a + 2l_{ew\text{-}f} = 339.46 \text{ mm} \quad (8)$$

Since numbers of wires in parallel are identical in DTP-SF and DTP-DS winding configurations, the cross-sectional area of DTP-SF windings is the same as that of DTP-DS windings. Hence, the phase resistance of DTP-SF windings can be estimated from the winding lengths of the two windings and the phase resistance of DTP-DS windings as

$$R_{DTP\text{-}SF} = \frac{l_f}{l_s} R_{DTP\text{-}DS} \approx 0.174363 \text{ Ohm} \quad (9)$$

Besides the difference in phase resistance, it also should be noticed that the total axial lengths of different windings are also different. Using the same simplification method above, the total axial length of short-pitched windings, $l_{ta\text{-}s}$, and that of full-pitched windings, $l_{ta\text{-}f}$, can be estimated as

$$l_{ta\text{-}s} = l_a + 2\frac{l_{cs\text{-}s}}{2} = 113.90 \text{ mm} \quad (10)$$

$$l_{ta\text{-}f} = l_a + 2\frac{l_{cs\text{-}f}}{2} = 126.51 \text{ mm} \quad (11)$$

Overall, the axial length and the phase resistance of different winding configurations are summarized in Table 3.

Table 3. Estimated key parameters of different winding configurations.

	ORG	DTP-SF	DTP-DS
Total axial length (mm)	113.9	126.51	113.9
Phase resistance (Ohm)	0.077	0.174363	0.154

As shown in Table 3, compared with DTP-DS windings, the phase resistance in DTP-SF machines is increased by 13.2%, and the total axial length is also raised by 11.1%. It is suggested that the DTP-DS winding configuration is better than the DTP-SF counterpart in efficiency and machine size because the higher phase resistance implies higher copper loss under the same phase currents and the longer axial length denotes the machine's larger size.

Based on the calculations shown above, it can be summarized that the total volumes of copper wires utilized in ORG and DTP-DS machines are identical because of the identical short-pitched windings equipped in them. However, the DTP-SF machine needs more copper wires—13.2% higher than the counterparts—due to the full-pitched windings. In other words, the cost of winding connections in the DTP-SF machine is higher than the other two counterparts. It should be mentioned that the analyses presented here are only based on estimations. The actual winding length and machine size can be further optimized in design and assembling processes. However, it can still be concluded that compared with the DTP-SF counterpart, the DTP-DS winding configuration has inherent advantages in winding resistance and machine size due to the short-pitched windings in it.

3. Electromagnetic Performance under Healthy Condition

To reveal the merits and demerits of different winding configurations, the electromagnetic performances of Toyota Prius 2010 machines with ORG, DTP-SF, and DTP-DS windings are analyzed using the FE analysis software, JMAG Designer. It should be mentioned that the FE analyses shown below are calculated based on 1/4 machine models, as shown in Figure 9. Because of the 48-slot/8-pole topology of the investigated proto-

type machine, the electrical periodicity within the machine is 4, which suggests that the flux distributions are identical every quarter machine. Setting the two sides of a quarter machine as master and slave boundary boundaries, the electromagnetic performance of different winding configurations can be obtained from the $\frac{1}{4}$ models with much less computation time.

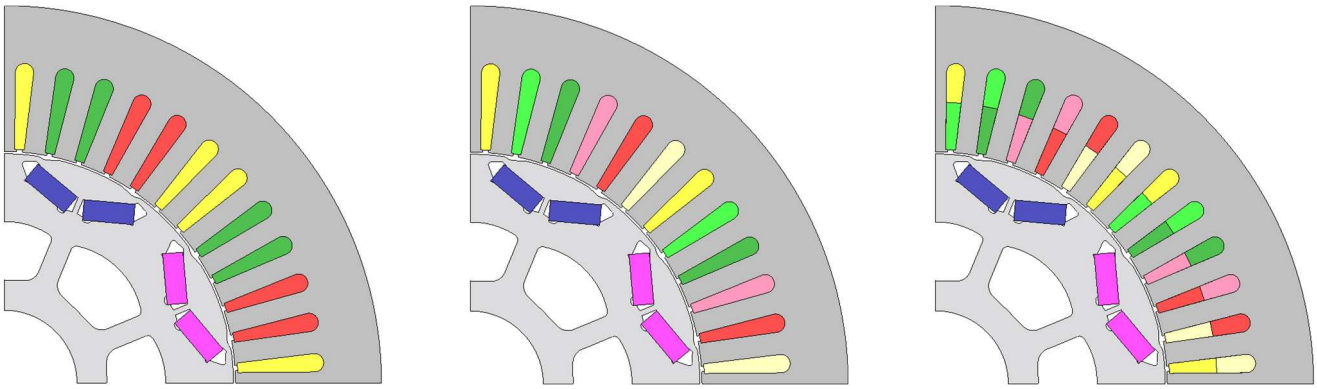

Figure 9. One-fourth models of Prius 2010 machine with different winding configurations: (**a**) ORG; (**b**) DTP-SF; (**c**) DTP-DS.

3.1. Winding Factor

For all winding configurations, the winding factor is the product of the distribution factor and the pitch factor. The distribution factors can be obtained from the coil EMF phasor diagrams shown in Figure 5, and the pitch factors are determined by slot/pole number combination and coil pitch number. In Figure 5a–c, it can be seen that the EMF phasors of the same phase overlap each other. Thus, the distribution factors of the three winding configurations are all 1. Pitch factors are the ratio of coil-pitch to pole-pitch. For the full-pitched windings in the DTP-SF machine, the pitch factor is 1. For the short-pitched windings in ORG and DTP-DS machines, the pitch factors are 0.966. Then, the winding factors of different winding configurations are calculated and listed in Table 4.

Table 4. Winding factors of different winding configurations.

	ORG	**DTP-SF**	**DTP-DS**
Distribution factor, k_d	1	1	1
Pitch factor, k_p	0.966	1	0.966
Winding factor, k_w	0.966	1	0.966

From Table 4, it can be concluded that the full-pitched windings in the DTP-SF machine improve the winding factor from 0.966 in the ORG machine to 1. The winding factor improvement is about 3.53%. In the DTP-DS machine, each winding set shares the same layout with ORG windings. Hence, the DTP-DS winding configuration cannot change the winding factors in the ORG machine.

However, it should be noticed that the winding factors shown in Table 4 only take the fundamental component in one winding set into consideration. In fact, there are two winding sets in DTP-SF and DTP-DS machines, and the resultant stator MMF and output torque are produced by the two winding sets containing abundant harmonic contents. It is necessary to evaluate the mutual effects of two winding sets between each other.

The ideal stator MMF distributions for ORG, DTP-SF, and DTP-DS winding configurations are calculated to illustrate the influences of the shifting windings on resultant stator MMF harmonics. The waveforms and spectra of ideal stator MMF distributions are shown in Figure 10a,b, respectively. Although ORG and DTP-DS winding configurations have different stator MMF distribution waveforms, the amplitudes of the fundamental components

in the two windings are identical. Compared with ORG and DTP-DS counterparts, the amplitude of the fundamental component in the DTP-SF winding configuration is higher, which agrees well with the calculated winding factors shown in Table 4. What is more, it can be seen that there are no fifth and seventh harmonics in DTP-SF and DTP-DS winding configurations from Figure 10b because these harmonics are eliminated by the two winding sets with a 30° phase shift. Furthermore, it can be inferred that the sixth torque pulsations can be totally eliminated in DTP-SF and DTP-DS machines [23].

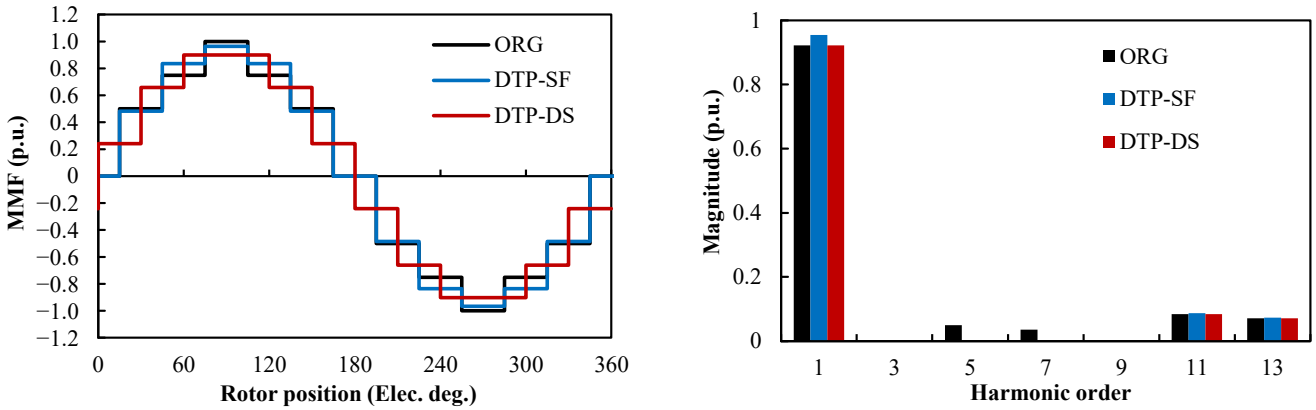

Figure 10. Ideal stator MMF distributions for different winding configurations: (**a**) waveforms; (**b**) spectra.

3.2. Open-Circuit (OC) Performance

3.2.1. Flux Distribution

Under OC conditions, all the flux in the machine is provided by permanent magnets in the rotor. Thus, different winding configurations have no influence on flux distribution performance. The flux density contour and the flux line distribution of the Prius 2010 machine under OC conditions are plotted in Figure 11a,b, respectively. The air-gap flux density waveform and its spectrum in the machine are shown in Figure 12a,b, respectively.

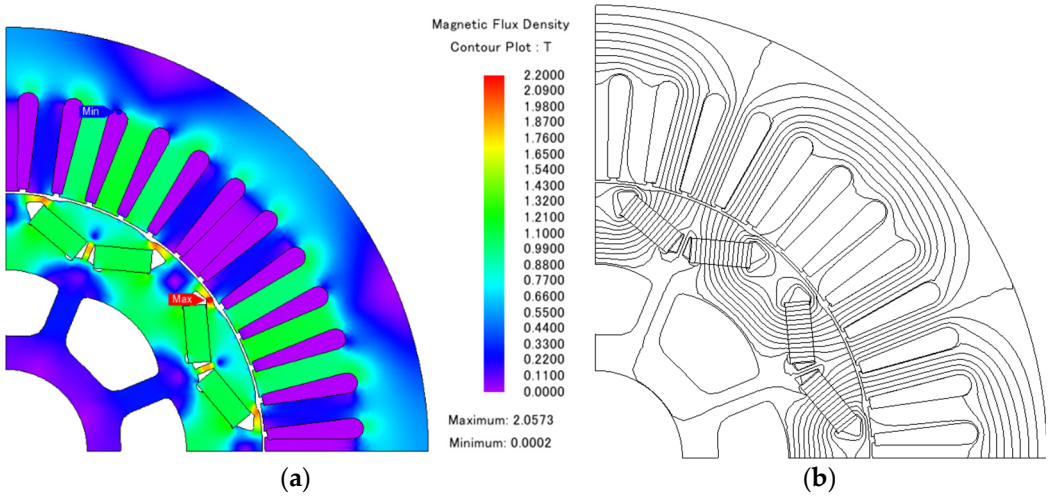

Figure 11. Flux distribution of Prius 2010 machine under OC condition: (**a**) contour; (**b**) flux line distribution.

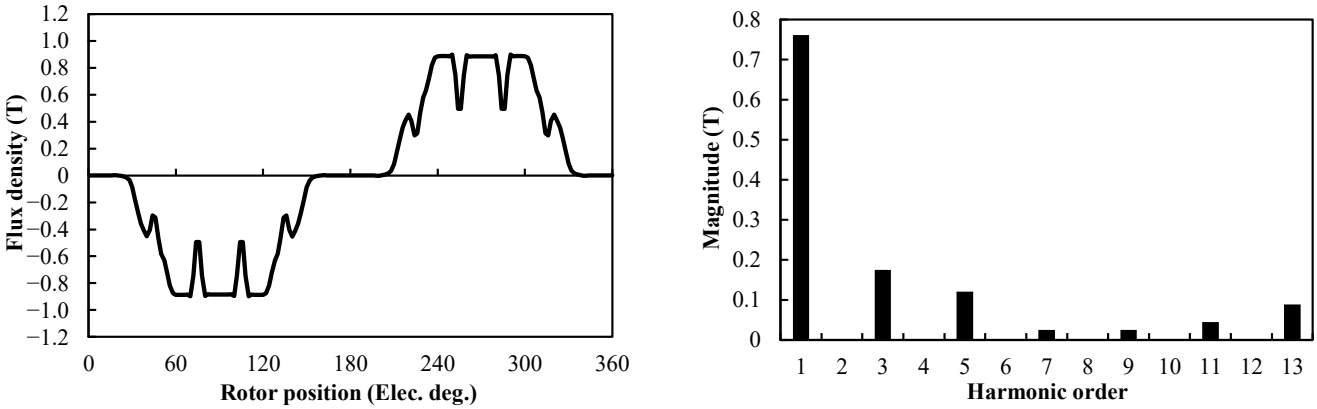

(a) (b)

Figure 12. Air-gap flux density distribution of Prius 2010 machine under OC condition: (**a**) waveform; (**b**) spectrum.

Although different winding configurations cannot affect the flux distribution performance of the machine under OC conditions, their flux linkages are different. The phase flux linkages of different winding configurations are presented in Figure 13a–c.

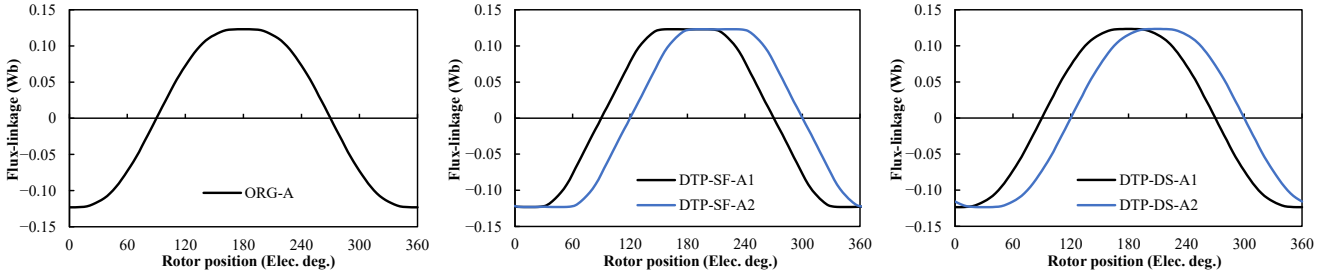

(a) (b) (c)

Figure 13. Phase flux-linkages of different winding configurations under OC condition: (**a**) ORG; (**b**) DTP-SF; (**c**) DTP-DS.

3.2.2. Back EMF

The waveforms of back EMFs of Phase A in ORG machine, Phases A1, A2 in DTP-SF and DTP-DS machines are shown in Figure 14 (Rotation speed is 3000 rpm). It can be clearly seen that the shifting angle between the two winding sets is 30° in DTP-SF and DTP-DS machines.

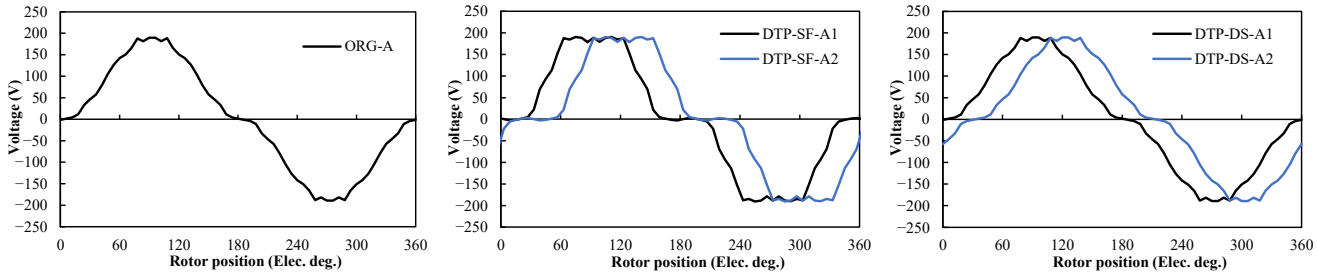

(a) (b) (c)

Figure 14. Phase back EMF of different winding configurations at 3000× g rpm: (**a**) ORG; (**b**) DTP-SF; (**c**) DTP-DS.

The waveforms and spectra of phase back EMFs with different winding configurations are compared in Figure 15. In Figure 15a, the back EMF curve of ORG windings is totally overlapped with that of DTP-DS windings. The spectra of these back EMFs are given

in Figure 15b. For DTP-SF winding configuration, the magnitudes of the first, fifth, and seventh harmonics are higher than those in the ORG machine. To be more specific, the fundamental component is increased by about 3.53%, which validates the calculation of winding factors, as shown in Table 4. From Figure 15, it also can be seen that the harmonic contents in ORG and DTP-DS windings are identical.

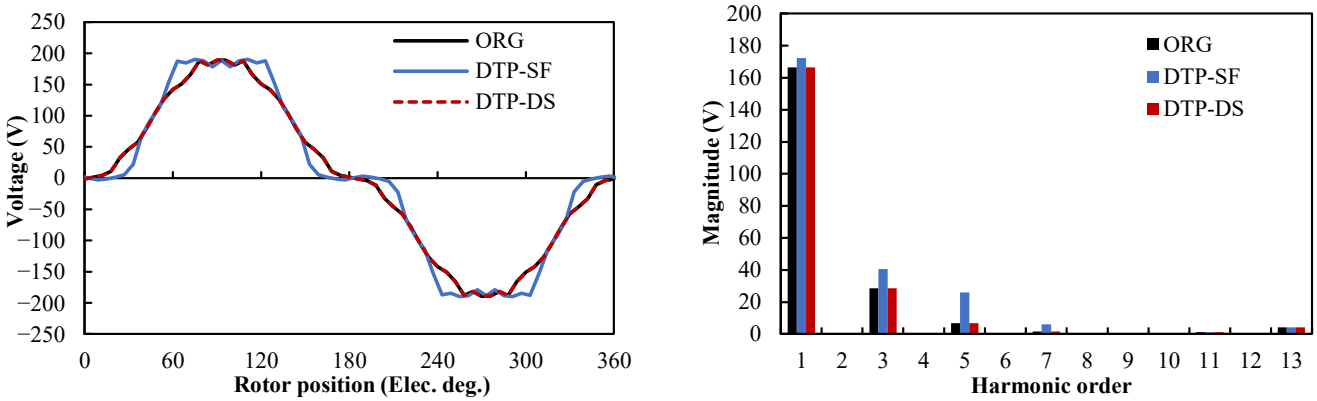

Figure 15. Phase back EMFs of different winding configurations at 3000× g rpm: (**a**) waveforms; (**b**) spectra.

The comparison of line-to-line back EMFs with different winding configurations is shown in Figure 16. The harmonic contents in line-to-line back EMFs are similar to those in phase back EMFs except that the triple harmonics (the third and ninth harmonics) are eliminated in line-to-line back EMFs due to the symmetric three-phase winding layouts.

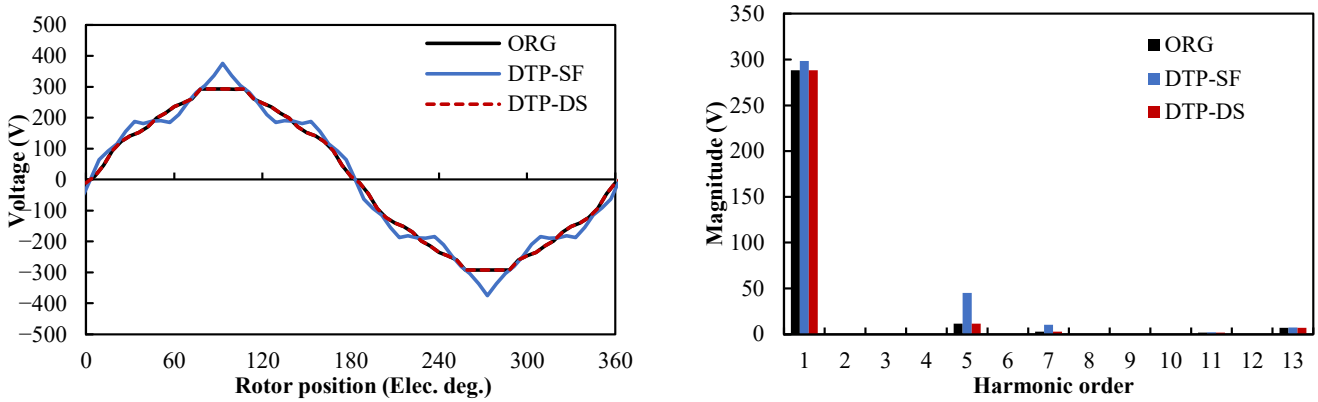

Figure 16. Line-to-line back EMFs of different winding configurations at 3000× g rpm: (**a**) waveforms; (**b**) spectra.

3.2.3. Cogging Torque

As cogging torque is not associated with armature currents, different winding configurations share the same cogging torque characteristic. The waveform and spectrum of the cogging torque in the Prius 2010 machine are shown in Figure 17a,b, respectively. It is illustrated that the dominant harmonic in cogging torque is the twelfth harmonic, which is the least common multiple between the slot number and pole pair number for a 48-slot/8-pole machine.

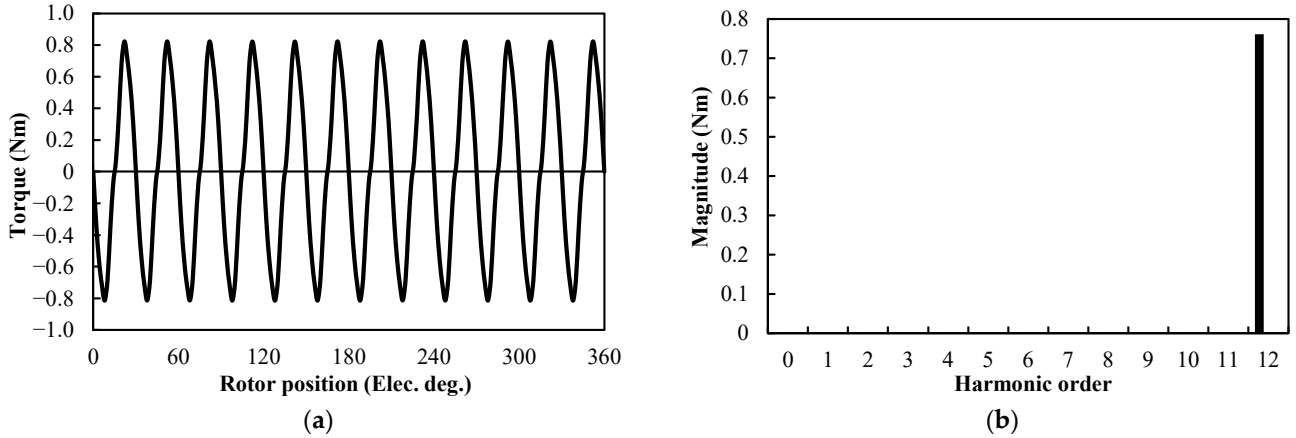

Figure 17. Cogging torque of Prius 2010 machine: (**a**) waveform; (**b**) spectrum.

3.2.4. Inductance Characteristics

The inductance characteristics of different winding configurations under OC conditions can also be obtained from these models. The d- and q-axis inductances of these winding configurations are shown in Figure 18a–c. It should be noticed that the frozen permeability method is utilized to improve the accuracy in inductance calculations, and the details can be found in [44]. From Figure 18a,c, it can be observed that the inductance characteristics of each winding set in DTP-DS windings are very similar to that of ORG windings. The oscillations of d- and q-axis inductances in DTP-SF windings are much larger than those in ORG and DTP-DS windings.

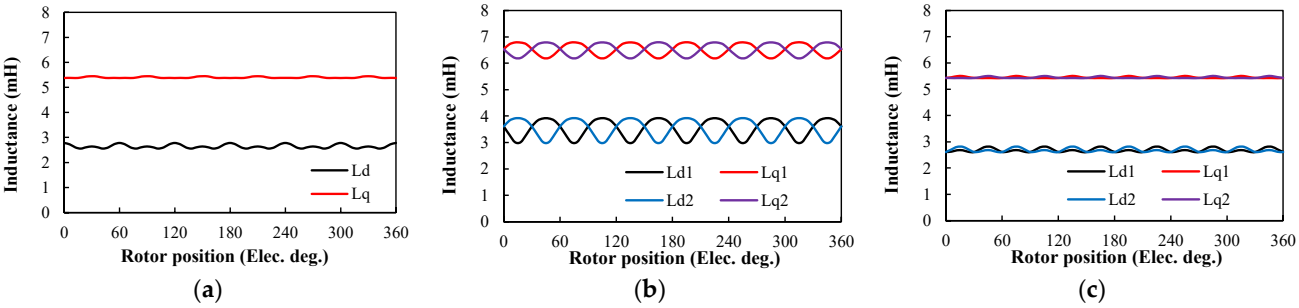

Figure 18. d- and q-axis inductances of different winding configurations at OC: (**a**) ORG; (**b**) DTP-SF; (**c**) DTP-DS.

3.3. Torque Performance

3.3.1. Average Torque-Current Advancing Angle Characteristics

Since an IPM rotor is employed in the Toyota Prius 2010 IPM machine, the output torque varies with the current advancing angle in windings, and the current advancing angle should be chosen specially to make full use of the electromagnetic and reluctance torque components in the machine. In this part, the variations of average torque with current advancing angle are examined with different winding configurations.

To produce the largest torque, the maximum phase currents are employed, which are 236 Apk in ORG windings and 118 Apk in DTP-SF and DTP-DS windings. In ORG windings, the current advancing angle is a variable, β. In DTP-SF and DTP-DS windings, the current advancing angles for the two winding sets are β_1 and β_2, respectively. Since β_1 and β_2 are displaced by 30°, it can be assumed that $\beta_1 = \beta + 15°$ and $\beta_2 = \beta - 15°$. Then, the output torques of STP and DTP machines are all varied with only β. The average torque-current advancing angle characteristics of different winding configurations are shown in Figure 19, and the specific values are given in Table 5. It can be seen that the maximum output torque is obtained when $\beta = 50°$ for all winding configurations. This indicates

that both DTP-SF and DTP-DS winding configurations do not change the optimal current advancing angle in the ORG machine. In other words, the optimal current advancing angle in the ORG machine can be utilized directly in DTP machines.

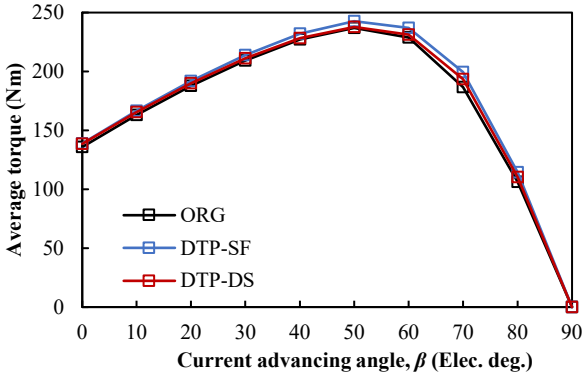

Figure 19. Average torque-current advancing angle characteristics of different winding configurations.

Table 5. Comparison of average torque-current advancing angle characteristics of different winding configurations.

	ORG	DTP-SF		DTP-DS	
Current Advancing Angle, β (ED)	Average Torque (Nm)	Average Torque (Nm)	Improvement (% Compared with ORG)	Average Torque (Nm)	Improvement (% Compared with ORG)
0	135.82	138.74	2.15	138.67	2.10
10	162.93	166.46	2.17	165.63	1.66
20	187.70	191.73	2.15	190.03	1.24
30	209.31	213.77	2.14	211.08	0.85
40	227.22	232.12	2.16	228.23	0.44
50	**236.98**	**242.80**	**2.45**	**237.75**	**0.33**
60	228.95	237.02	3.53	231.26	1.01
70	186.77	199.38	6.75	193.43	3.57
80	106.29	114.43	7.66	110.36	3.83
90	0.01	0.02	-	0.05	-

From Figure 19 and Table 5, it is expected that the DTP-SF winding configuration has a relatively higher torque output capacity than other counterparts because it has a higher winding factor.

For the DTP-DS winding configuration, although it shares identical winding factors with the ORG counterpart, the torque characteristics of the two winding configurations are not the same. The average torque of the DTP-DS machine is slightly higher than that of the ORG counterpart. In other words, the average torque in the ORG machine can be improved slightly using the DTP-DS winding configuration.

To be specific, in Table 5, Row 1, the torque improvements in DTP-SF and DTP-DS machines at 0 current advancing angle are 2.15% and 2.10%, respectively, compared with the ORG counterpart. In Section 3.1, it is mentioned that DTP winding configurations can produce different stator MMFs. It is assumed that DTP winding configurations affect the flux distributions a lot, and consequently, improve the average torque. To investigate the influences of different winding configurations on flux distributions, the flux density contours of these winding configurations under this condition are shown in Figure 20. It can be observed that the influences of winding configurations on flux distributions are very minor. The air-gap flux density waveforms and spectra of these winding configurations under this condition are shown in Figure 21. It can also be seen that the air-gap flux density distributions of different winding configurations are very similar to each other. From Figures 20 and 21, it can be summarized that the influences of DTP windings on the overall

flux distributions are very minor. The torque improvements of DTP winding configurations cannot be attributed simply to the different flux distributions in DTP machines. However, although the different stator MMF cannot be easily observed in Figures 20 and 21, the elimination of the harmonic contents in the stator's MMF still results in lower eddy currents in the magnets. Thus, the magnet eddy loss can be reduced in DTP machines, as will be shown later.

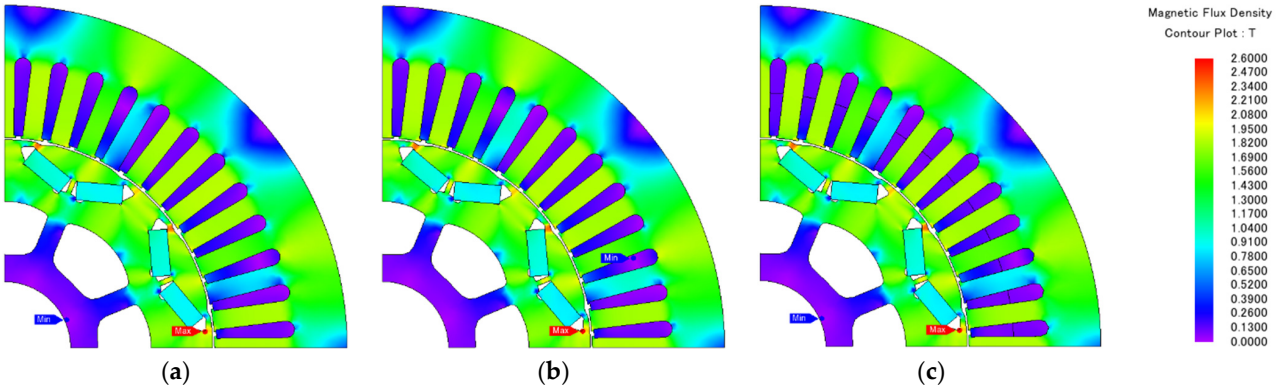

Figure 20. Flux density distributions of different winding configurations at I_A = 236 Apk, β = 0°: (**a**) ORG; (**b**) DTP-SF; (**c**) DTP-DS.

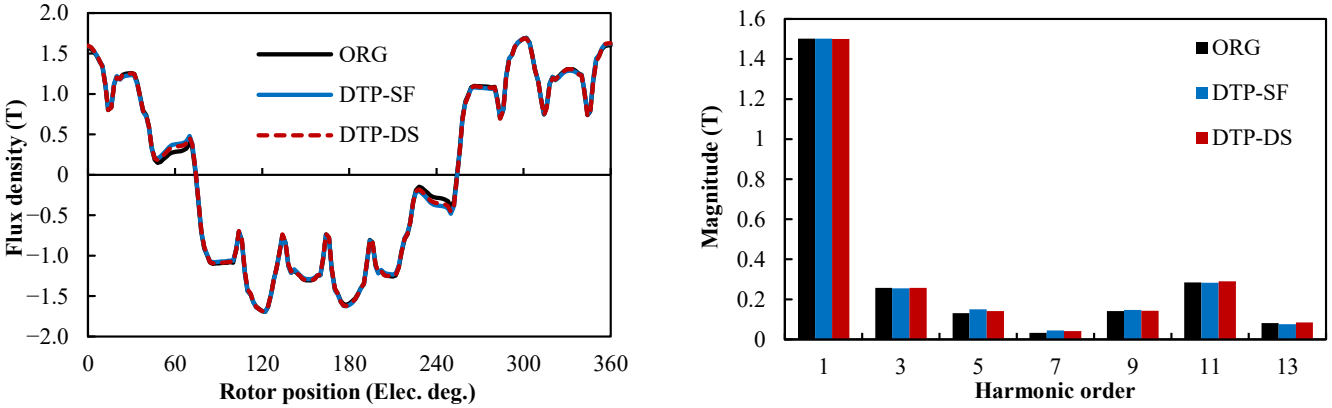

Figure 21. Air-gap flux density distributions of different winding configurations at I_A = 236 Apk, β = 0°: (**a**) waveforms; (**b**) spectra.

It should be noticed that the air-gap flux density distributions shown in Figure 21 are captured at a specific time. To illustrate the variation in air-gap flux density distributions over a whole electrical period, the waveforms and spectra of phase back EMFs of different winding configurations are shown in Figure 22. In Figure 22, the higher fundamental back EMF in the DTP-SF machine can be observed as the DTP-SF winding configuration has a higher fundamental winding factor. It also can be observed the fifth and seventh harmonics are reduced in the DTP-DS machine. Although the flux contours and air-gap flux density distributions look similar in ORG and DTP-DS machines, their harmonic contents are not exactly the same. Some MMF harmonics (particularly the fifth and seventh) can be reduced using the DTP-DS winding configuration.

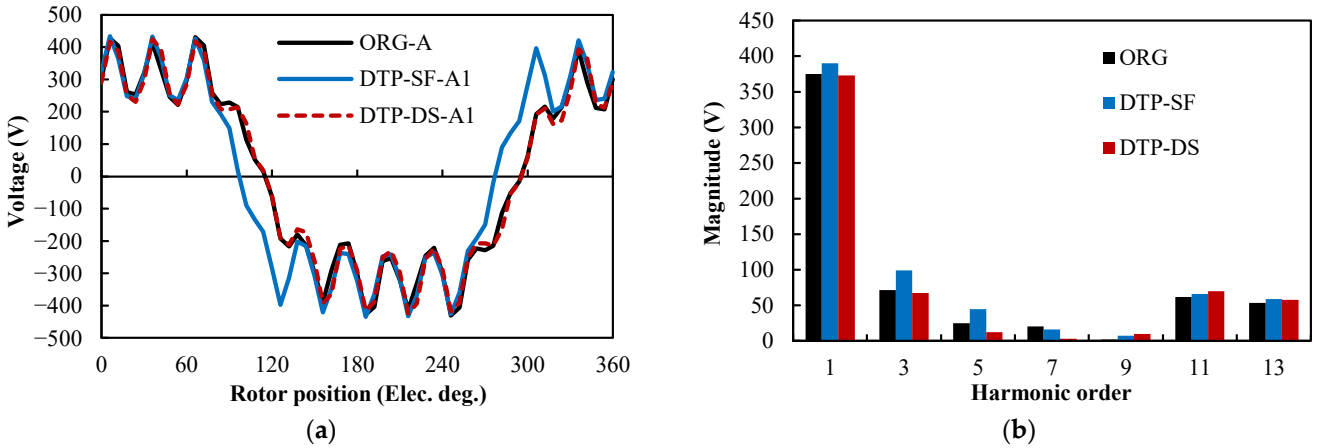

Figure 22. Phase back EMFs of different winding configurations @I_A = 236 Apk, $\beta = 0°$: (**a**) waveforms; (**b**) spectra.

Additionally, as only one phase is considered in Figure 22, it is necessary to take all phases into consideration. Multiplying the phase back EMF and phase currents, the input power of the machine can be obtained, as shown in Figure 23. The average input power of ORG, DTP-SF and DTP-DS machines are 55.43 kW, 57.46 kW, and 56.21 kW, respectively. Compared with ORG winding configuration, the power improvements in DTP-SF and DTP-DS counterparts are 3.65% and 1.40%, respectively.

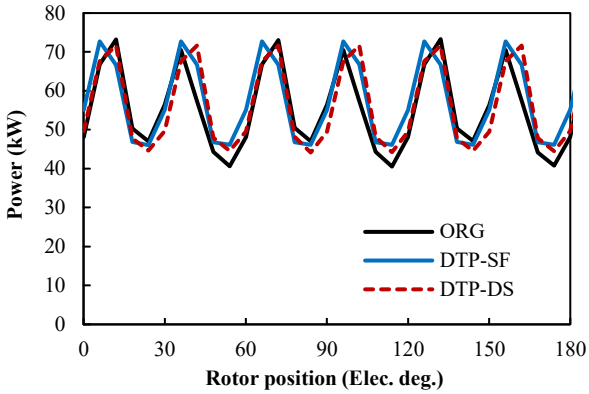

Figure 23. Input power of different winding configurations @I_A = 236 Apk, $\beta = 0°$.

From Figures 22 and 23, it can be summarized that although the influences of two winding sets on flux distributions cannot be observed clearly in Figures 20 and 21, the two winding sets can truly reduce some harmonic contents and improve the overall input power.

In general, the average torque improvement of the DTP-DS winding configuration should be attributed to the two winding sets with reduced MMF harmonics. The reduced MMF harmonic contents improve total input and reduce magnet eddy current loss in the machine. The detailed loss calculation will be presented in Section 3.4.1. As a result, although the DTP-DS winding configuration shares the same winding factors with the ORG machine, the average torque of the ORG machine can still be improved a little by using DTP-DS windings.

3.3.2. Instantaneous Torque Characteristics

According to Figure 19, the maximum torque condition of different winding configurations is selected for further analyses. The instantaneous torque waveforms are shown in Figure 24a, and their spectra are given in Figure 24b. The average torque and torque ripple of different winding configurations are listed in Table 6. It can be seen that not only the average torque is improved by DTP winding configurations, but also the torque ripples are

reduced significantly by using DTP windings. To be specific, the torque ripple in the ORG machine is 14.59%, while it is 8.43% in DTP-SF and 7.80% in DTP-DS counterparts.

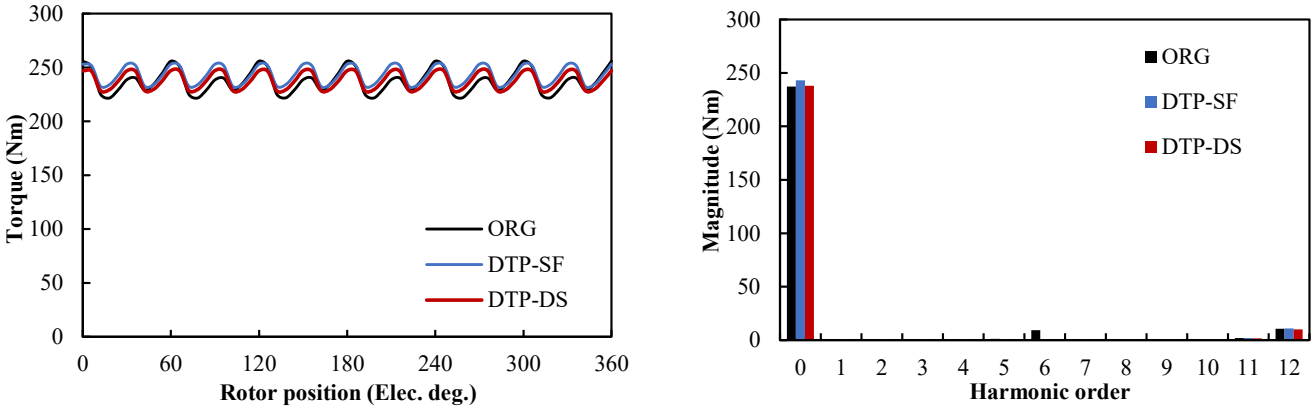

(**a**) Waveforms (**b**) Spectra

Figure 24. Instantaneous torque performance of different winding configurations under maximum torque condition: (**a**) waveforms; (**b**) spectra.

Table 6. Comparison of instantaneous torque performance of different winding configurations under maximum torque condition.

	ORG	DTP-SF	DTP-DS
Average torque	236.98	242.80	237.75
Improvement (% compared with ORG)	-	2.45	0.33
Torque ripple (Nm)	34.11	20.46	18.54
Torque ripple (%)	14.39	8.43	7.80

From Figure 24b, it can be seen that the dominant torque harmonics in the ORG machine are the sixth and twelfth harmonics. As suggested in Figure 10, with the utilization of DTP windings with a 30° phase shift, the sixth torque harmonics are totally eliminated. Thus, the torque ripples in DTP-SF and DTP-DS machines are much lower than that in the ORG machine. In other words, both DTP-SF and DTP-DS winding configurations can reduce torque ripple significantly.

The inductance characteristics of the three winding configurations under the maximum torque condition also can be calculated using the method proposed in [44]. The d- and q-axis inductances in the three machines are shown in Figure 25. Compared with the inductances at OC condition shown in Figure 18, both d- and q-axis inductances are affected obviously by the load. The q-axis inductances are reduced significantly in all three machines. The fluctuations of all inductances with rotor position are much more evident due to the relatively severe magnetic saturation in the machine under the maximum torque condition.

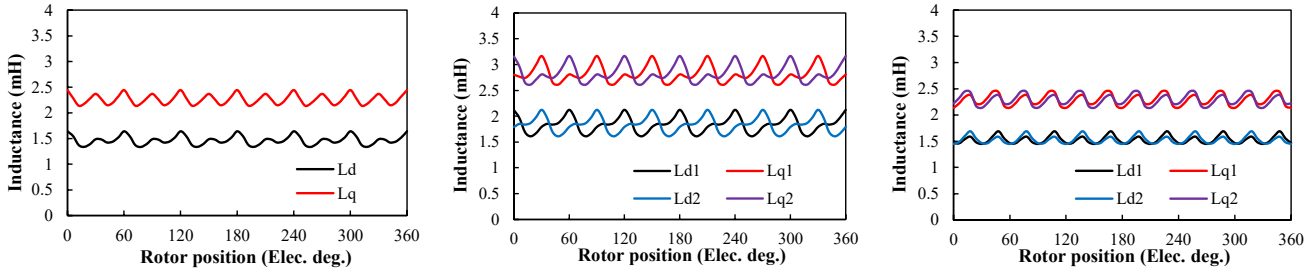

(**a**) (**b**) (**c**)

Figure 25. d- and q-axis inductances of different winding configurations at maximum torque condition: (**a**) ORG; (**b**) DTP-SF; (**c**) DTP-DS.

Besides the maximum torque condition, the variations of d- and q-axis inductances with different excitation conditions are also calculated [45], as shown in Figure 26. It should be noticed that frozen permeability method is not utilized in the calculation to obtain Figure 26. In Figure 25, it can be seen that the d- and q-axis inductances in DTP-SF, Figure 25b, are higher than those in DTP-DS windings, Figure 25c. However, in Figure 26, the inductance characteristics of the three winding configurations are almost the same because the mutual inductances are not considered fully in the method proposed in [45]. From Figure 26, it still can be inferred that the magnetic saturations in the three machines are very similar to each other, as shown in Figure 20. It also can be observed that both d- and q-axis currents can affect d- and q-axis inductances very evidently.

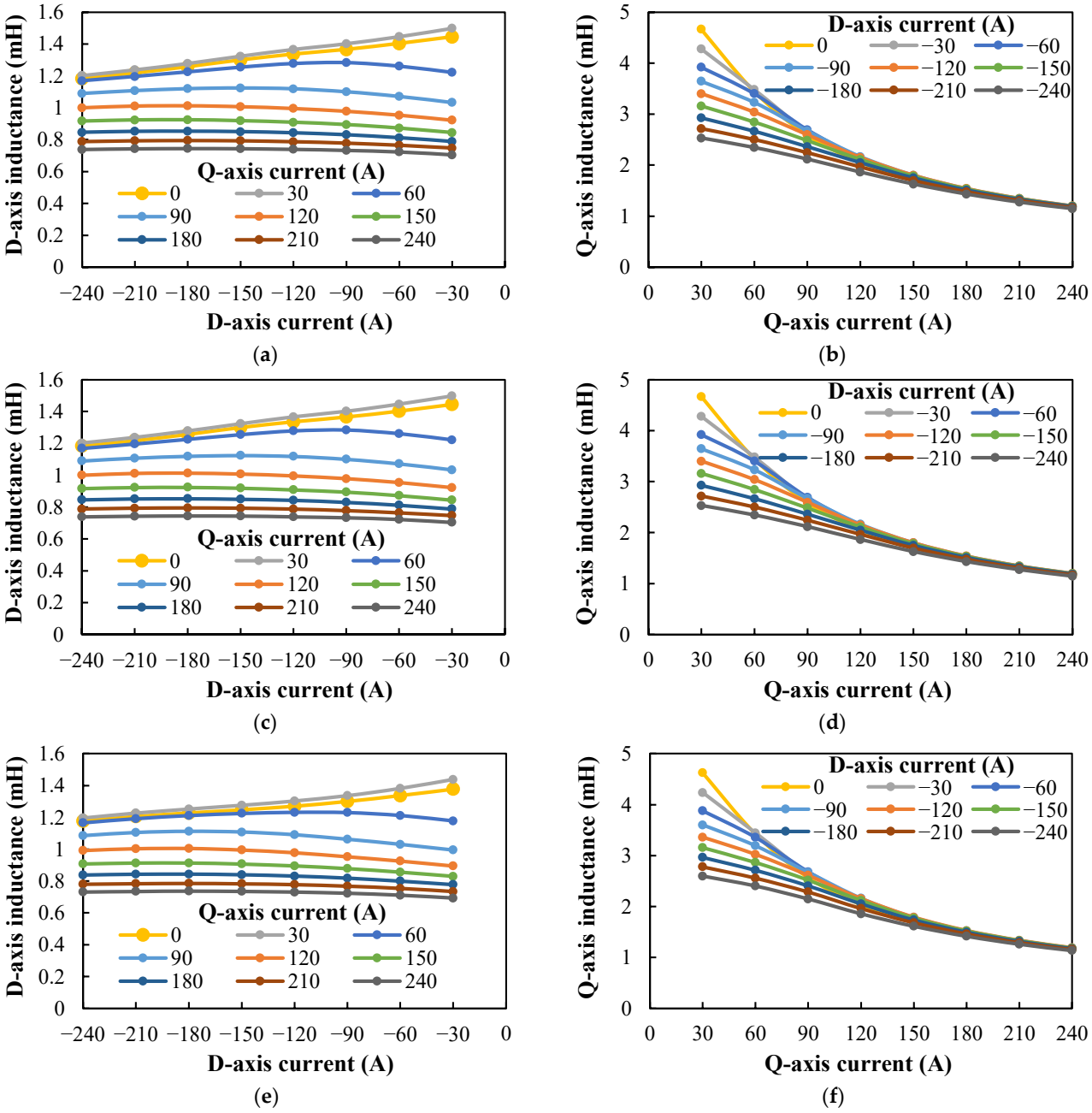

Figure 26. Variations of d- and q-axis inductances with different winding configurations and different d- and q-axis current combinations: (**a**) ORG: d-axis inductance; (**b**) ORG: q-axis inductance; (**c**) DTP-SF: d-axis inductance; (**d**) DTP-SF: q-axis inductance; (**e**) DTP-DS: d-axis inductance; (**f**) DTP-DS: q-axis inductance.

3.3.3. Average Torque and Torque Ripple–Current Amplitude Characteristics

Besides the maximum torque condition, the torque characteristics of these winding configurations under different excitation conditions are also investigated in this paper. It has been mentioned previously that since the number of turns is doubled in DTP winding configurations, the phase currents in DTP windings should be halved from those in ORG windings to keep the same Ampere-turns output. Assuming that the phase current amplitude in ORG windings is I_A, the phase current amplitude in DTP-SF and DTP-DS machines is $I_A/2$. If the machine is controlled using the maximum torque per ampere (MTPA) strategy, β is always selected particularly to produce the largest torque. With I_A varying from 10A, 50A, 100A, 150A, 200A to 236A, the average torque and torque ripple of different winding configurations are plotted in Figure 27. The detailed values of average torques and torque ripples are listed in Table 7.

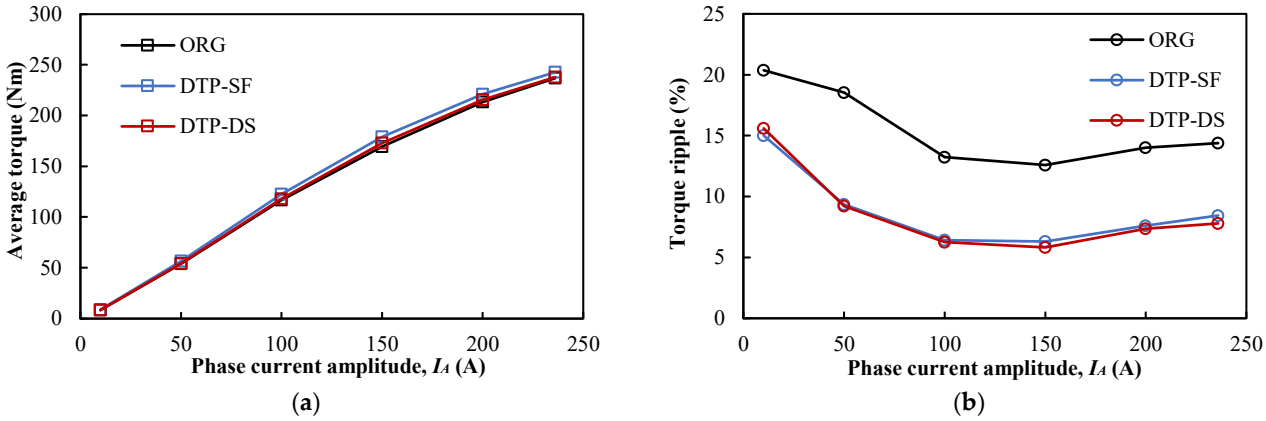

Figure 27. Torque-current amplitude characteristics of different winding configurations with MTPA strategy: (**a**) average torque; (**b**) torque ripple.

Table 7. Comparison of torque-current amplitude characteristics of different winding configurations with the MTPA strategy.

I_A (A)		ORG	DTP-SF	DTP-DS
10	Average torque (Nm)	8.25	8.55	8.25
	Improvement (% compared with ORG)		3.73	−0.02
	Torque ripple (Nm)	1.68	1.28	1.29
	Torque ripple (%)	20.37	15.00	15.59
50	Average torque	54.01	56.52	54.17
	Improvement (% compared with ORG)		4.64	0.29
	Torque ripple (Nm)	10.02	5.29	5.00
	Torque ripple (%)	18.55	9.36	9.23
100	Average torque	116.66	122.44	117.95
	Improvement (% compared with ORG)		4.95	1.10
	Torque ripple (Nm)	15.43	7.84	7.39
	Torque ripple (%)	13.22	6.41	6.26
150	Average torque	169.44	178.90	172.86
	Improvement (% compared with ORG)		5.59	2.02
	Torque ripple (Nm)	21.32	11.27	10.08
	Torque ripple (%)	12.58	6.30	5.83
200	Average torque	213.38	221.15	215.64
	Improvement (% compared with ORG)		3.64	1.06
	Torque ripple (Nm)	29.91	16.83	15.88
	Torque ripple (%)	14.02	7.61	7.37
236	Average torque	236.98	242.80	237.75
	Improvement (% compared with ORG)		2.45	0.33
	Torque ripple (Nm)	34.11	20.46	18.54
	Torque ripple (%)	14.39	8.43	7.80

According to Table 7, when the currents are very small (I_A = 10A), the torque improvements of DTP-SF and DTP-DS winding configurations are 3.73% and −0.02%, respectively, which agree very well with the theoretical improvements on winding factors. Except for this condition, both DTP-SF and DTP-DS winding configurations can improve average torque and reduce torque pulsation at the same time. To be more specific, the torque improvement in the DTP-SF winding configuration is higher than that in the DTP-DS counterpart, while the torque pulsation in the DTP-DS machine is always slightly lower than that in the DTP-SF machine. It is noteworthy that the torque improvements of DTP-SF and DTP-DS winding configurations are 5.59% and 2.02%, respectively, under the condition I_A = 150 A. The actual torque improvements are much higher than the theoretical values (3.53% in DTP-SF winding configuration and 0% in DTP-DS winding configuration). This indicates that the real torque improvement caused by DTP windings can be much higher than the theoretical increase in winding factors under specific on-load conditions.

3.3.4. Torque and Power–Speed Characteristics

In the analyses above, the speed of the machine is fixed at 3000 rpm. The performances of different winding configurations under different speeds, especially high-speed conditions, have not been considered. In this part, to illustrate the influences of DTP-SF and DTP-DS winding configurations on the Toyota Prius 2010 IPM machine over the entire speed range, the torque and power-speed envelopes of different winding configurations are shown in Figure 28. In the calculation, the DC voltage is fixed at 650 V, and the phase currents are limited at 236 Apk in STP windings and 118 Apk in DTP windings. It should be mentioned that the power shown in Figure 28b is the output power of these machines. A comparison of input powers of different winding configuration machines should take losses into consideration, which will be presented in the next part. According to the calculation results, the base speed is 3500 rpm, 3400 rpm, and 3600 rpm in ORG, DTP-SF, and DTP-DS machines, respectively. Thus, the DTP-DS winding configuration can increase the base speed a little.

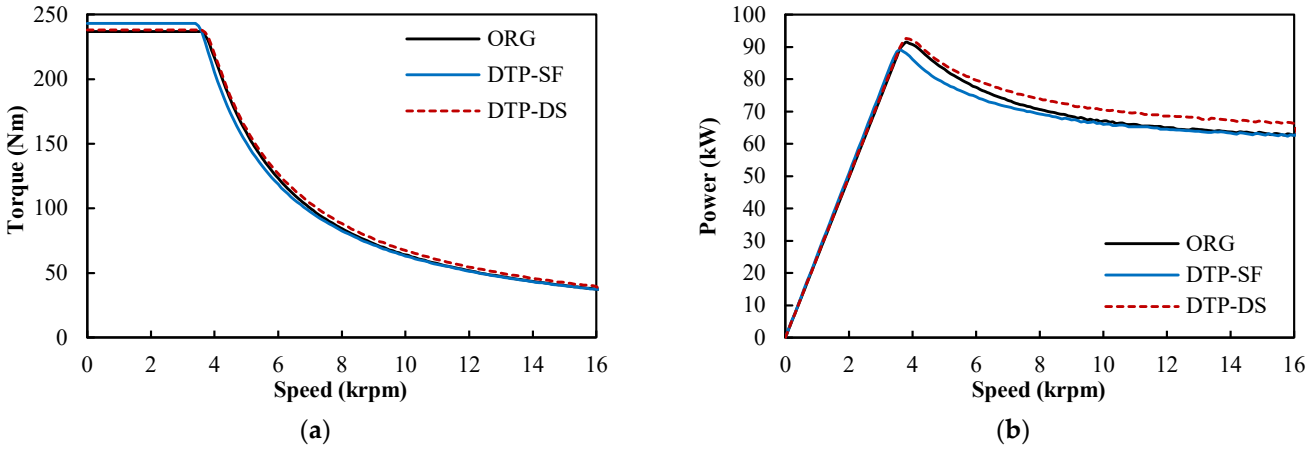

Figure 28. Torque– and power–speed envelopes of different winding configurations: (**a**) torque–speed envelope; (**b**) power–speed envelope.

In the constant torque range, the DTP-SF winding configuration shows the highest output torque. ORG and DTP-DS winding configurations have very similar output torque capacities. However, when the speed is higher than the base speed, the machine is run in the constant power range. The output power of the DTP-SF winding configuration is lower than that of the ORG counterpart, and the DTP-DS winding configuration has the highest output power. Since higher output power suggests higher output torque with the same rotation speed, the DTP-DS winding configuration produces the largest torque under high-speed conditions.

To further find out the reason why the DTP-DS winding configuration can produce the highest torque in the high-speed range, the phase currents in these winding configurations to produce the highest torque should be calculated and compared.

In fact, in the calculation of the torque– and power–speed envelopes shown in Figure 28, the d- and q-axis currents that produce the maximum torque at different speed conditions have been obtained, as shown in Figure 29. Firstly, the torque– and power–speed envelopes are calculated based on 81 cases with different d- and q-axis currents at a specific speed, 3000 rpm. In the 81 cases of the ORG machine, the d-axis current is varied from 0A to −240A and the q-axis current is varied from 0A to 240A. In the cases of DTP-SF and DTP-DS machines, d- and q-axis currents are varied from 0A to −120A and 0A to 120A, respectively. Thus, the variations of d- and q-axis flux-linkages over the entire excitation range ($-240\text{A} \leq I_d \leq 0\text{A}$ and $0\text{A} \leq I_q \leq 240\text{A}$ in ORG machine; $-120\text{A} \leq I_d \leq 0\text{A}$ and $0\text{A} \leq I_q \leq 120\text{A}$ in DTP-SF and DTP-DS machines) at 3000 rpm can be obtained using the interpolation function. Then, the variation of output torque over the excitation range can be obtained from the d- and q-axis flux-linkages and corresponding currents. Then, since output torque keeps the same under the same excitation condition regardless of rotation speed, the variation of output torque at 3000 rpm can be utilized at any speed condition. Different from that in output torque, phase back EMF is closely related to rotation speed. Taking speed, flux-linkages, currents, and phase resistance into consideration, the variation of phase back EMF over the entire excitation range at different speed conditions also can be calculated. When the speed is lower than the base speed of the machine, the d- and q-axis currents are selected to produce the highest torque under the current amplitude limit. When the speed is higher than the base speed of the machine, the d- and q-axis currents are selected to produce the highest torque under the limit of DC-link voltage.

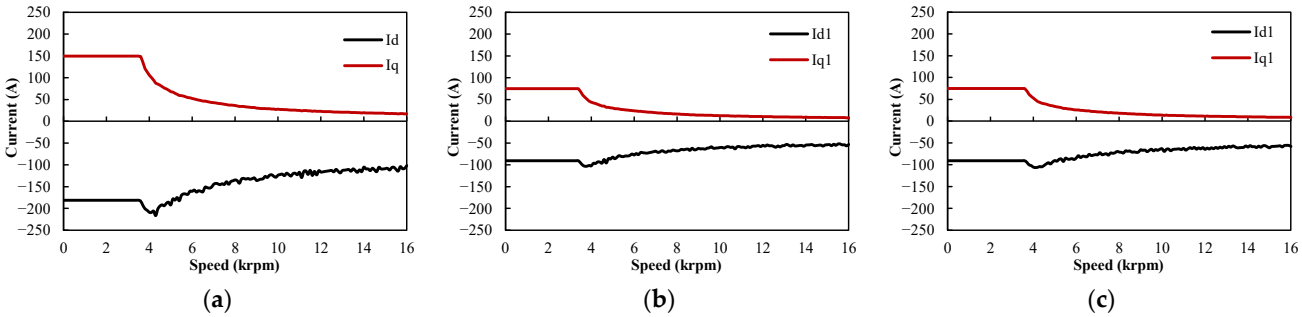

Figure 29. d- and q-axis currents of different winding configurations over entire speed range: (**a**) ORG; (**b**) DTP-SF; (**c**) DTP-DS.

According to the d- and q-axis currents shown in Figure 29, the amplitudes and current angles of phase currents in the three windings over the entire speed range are shown in Figure 30a,b. It should be mentioned that the phase current amplitudes in DTP-SF and DTP-DS windings are doubled in Figure 30a to make the comparison clearer. It also can be observed that the curves shown in Figure 30 are not very smooth because the number of cases used in the calculation is only 81. The variations of phase back EMF and torque over the entire excitation range are fitted based on 81 cases, which resulted in some small errors between estimated values and real results. These small errors cause the small pulsations in the current amplitude– and current angle–speed curves in Figure 30.

From Figure 30a,b, it can be found that the amplitudes of phase currents in DTP-DS windings are higher than those in DTP-SF and ORG windings, while the current angles of different winding configurations are very similar. It is inferred that the lower winding factor and reduced MMF harmonics decrease the amplitude of back EMF in DTP-DS windings. In high-speed conditions, the constraint is DC-link voltage, the lower back EMF suggests that the higher phase currents can be utilized, and the higher phase currents in DTP-DS windings result in larger output torque in the DTP-DS machine than other counterparts over the constant power range.

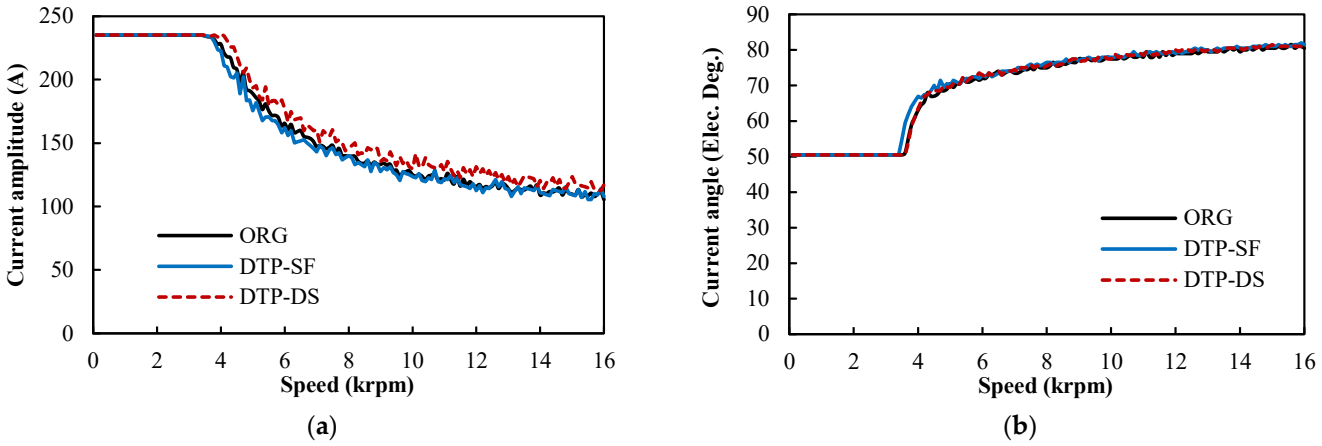

Figure 30. Amplitudes and current angles of phase currents of different winding configurations over entire speed range: (**a**) amplitudes; (**b**) current angles.

Overall, it can be concluded that the DTP-SF winding configuration can improve average torque in the constant torque range and the DTP-DS winding configuration can improve average torque in the constant power range, although both are not very significant.

3.4. Loss and Efficiency Performance

3.4.1. Loss and Efficiency under the Maximum Torque Condition

The losses of different winding configurations under the maximum torque conditions are calculated firstly. The total loss in a PMSM machine can be classified into copper loss, iron loss, PM eddy loss, and mechanical loss. Copper loss is calculated using Joule's law. Iron loss and PM eddy loss are calculated by the FE software, JMAG, according to the properties of materials. The lamination material used in the model is '35H270', and the PM material is 'NdFeB_Br = 1.2T'.

Although different winding configurations are utilized, the mechanical structures of these machines are identical. Hence, all the three winding configurations share the same mechanical loss characteristics, which are estimated using the measured results in [40], as shown in (12) and Figure 31.

$$P_{me}(f) = 0.26f + 0.00103f^2 \quad (12)$$

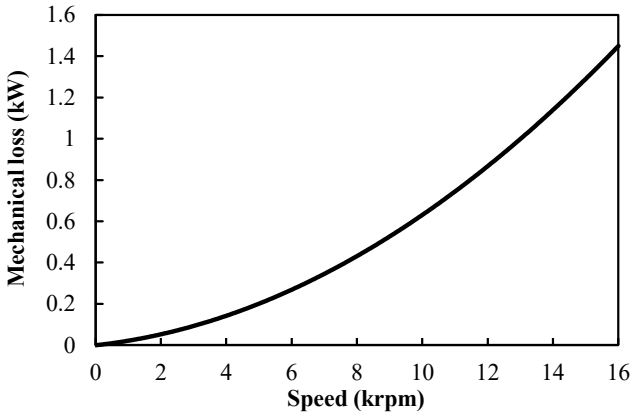

Figure 31. Variation of mechanical loss with speed [40].

With the methods mentioned above, the losses of different winding configurations under the maximum torque condition are calculated. Then, the efficiencies of machines with different winding configurations are obtained. The losses and efficiencies are summarized in Table 8. It can be seen that copper loss is the dominant loss among all kinds of losses. Compared with ORG and DTP-DS winding configurations, the larger resistance of

full-pitched windings in DTP-SF winding configuration results in higher copper loss and lower efficiency. From Table 8, it can also be seen that the PM eddy loss can be reduced significantly by using DTP windings. This phenomenon can be explained by the reduced stator MMF harmonics in DTP winding configurations. However, PM eddy loss is much smaller than copper loss. The reduction in PM eddy loss in the DTP-DS winding configuration can only increase its efficiency very little, but it may affect the rotor temperature significantly. As PM eddy current loss accounts for a small part of the total loss in all investigated machines, the PM eddy current loss is neglected in this paper in order to significantly simplify the calculation of efficiency maps.

3.4.2. Loss and Efficiency Maps

Based on the calculations above, the losses and efficiencies of different winding configurations under the entire speed range can be obtained. The copper loss maps and iron loss maps of these winding configurations are calculated first, as shown in Figures 32 and 33, respectively.

Table 8. Loss and efficiency of different winding configurations under maximum torque condition.

	ORG	DTP-SF	DTP-DS
Speed (rpm)	3000	3000	3000
Average torque (Nm)	236.98	242.80	237.75
Copper loss (W)	6432.89	7283.49	6432.89
Iron loss (W)	358.34	368.14	365.40
PM eddy loss (W)	**94.58**	**46.24**	**51.28**
Mechanical loss (W)	93.20	93.20	93.20
Output power (W)	74449.61	76276.54	74690.46
Total loss (W)	6979.01	7791.07	6942.77
Input power (W)	81428.62	84067.61	81633.23
Efficiency (%)	91.43%	90.73%	91.50%

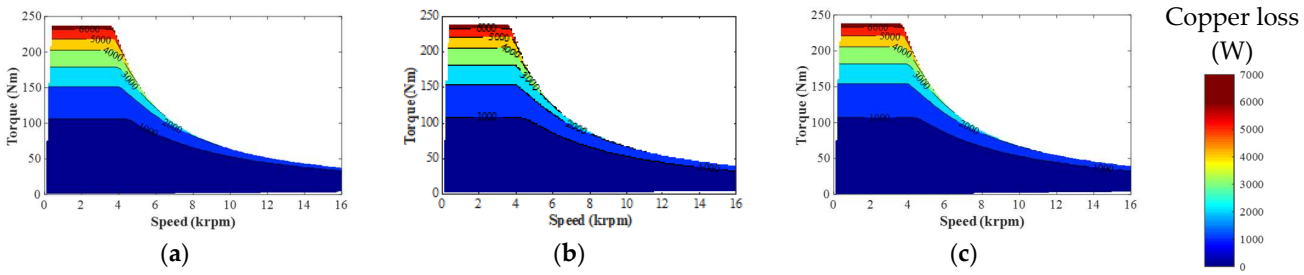

Figure 32. Copper loss maps of different winding configurations. (**a**) ORG; (**b**) DTP-SF; (**c**) DTP-DS.

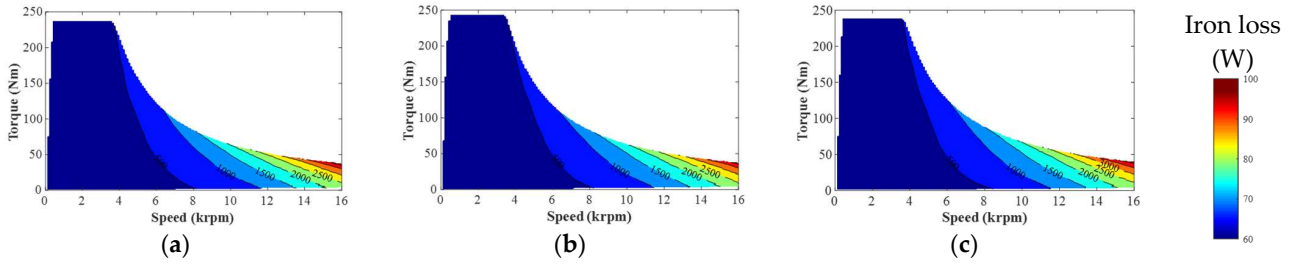

Figure 33. Iron loss maps of different winding configurations: (**a**) ORG; (**b**) DTP-SF; (**c**) DTP-DS.

Thus, the efficiency maps of different winding configurations are shown in Figure 34. It can be seen that the highest efficiency in ORG and DTP-DS winding configurations can reach 97%, while the highest efficiency in DTP-SF is 96%. The high-efficiency island in the DTP-DS machine is slightly larger than that in the ORG machine.

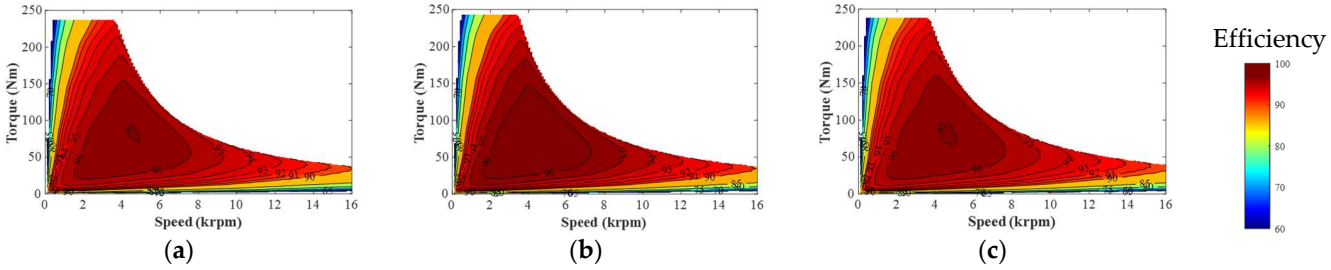

Figure 34. Efficiency maps of different winding configurations: (**a**) ORG; (**b**) DTP-SF; (**c**) DTP-DS.

The differences between the efficiency maps of DTP and ORG winding configurations are shown in Figure 35. For the DTP-SF winding configuration, the difference is negative in the most efficient region. However, for the DTP-DS winding configuration, the difference is positive in most of the whole range. It indicates that the efficiency of the DTP-SF winding configuration is lower than that of the ORG counterpart in most conditions, while the DTP-DS winding configuration can improve efficiency over most of the whole operating region. It also should be noticed that almost all differences shown in Figure 35 are lower than $\pm 0.5\%$, which suggests that the influences of DTP-SF and DTP-DS winding configurations on efficiency are not obvious.

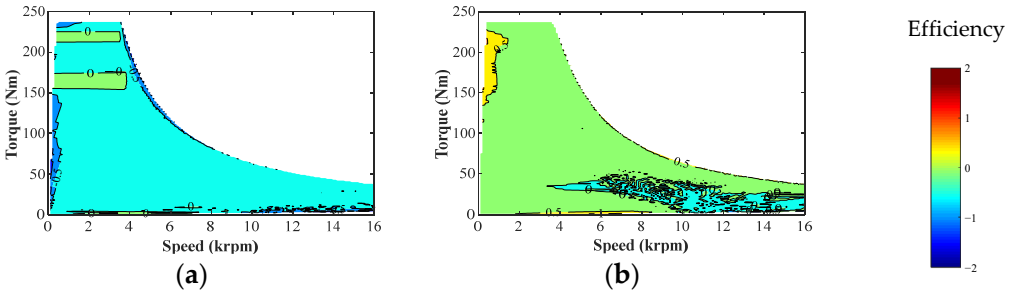

Figure 35. Differences between efficiency maps of DTP and ORG winding configurations: (**a**) DTP-SF; (**b**) DTP-DS.

3.5. Summary

In this section, the electromagnetic performances of ORG, DTP-SF, and DTP-DS winding configurations are compared comprehensively using the FE method. The comparison includes back EMF performance, torque and power characteristics, and efficiency performance. In each comparison, various characteristics are considered. From the analyses above, it is found that both DTP-SF and DTP-DS winding configurations can improve average torque and reduce torque ripples in the Toyota Prius 2010 IPM machine. Specifically, the DTP-SF winding configuration is more suitable for the constant torque range, as the torque improvement in the DTP-SF winding configuration is higher than that in the DTP-DS counterpart. The DTP-DS winding configuration is preferred for constant power range because it can produce higher output torque with lower torque pulsation in high-speed conditions.

4. Electromagnetic Performance under 3-ph OC Condition

The fault tolerance capability is a prominent advantage of the DTP winding configurations. Since DTP windings are composed of two separate three-phase winding sets, the failure of one winding set will not lead to the failure of the whole system, and DTP machines can only run with one three-phase winding set. The condition that one three-phase winding set is excited and one three-phase winding set is open-circuited is designated as the '3-ph OC condition' in this paper. Although the performance under the 3-ph OC condition indicates the fault-tolerant capability of the DTP machines, the '3-ph OC condition' does not always mean fault condition. When peak performance is not required, it is possible

to only partially excite the machine to improve efficiency by reducing copper, iron and inverter (switching and conduction) losses. Hence, better electromagnetic performance under the 3-ph OC condition even denotes more than just better fault-tolerant capability.

4.1. Winding Layouts

Firstly, assuming one of the two winding sets in DTP-SF and DTP-DS machines are open-circuited, the layouts of the remaining winding set are shown in Figure 36. It can be observed that the opposite parts of the stator are wound by the same phase windings. Thus, the radial forces produced by the opposite windings are balanced, and there will be no unbalanced radial force in the two machines under the three-phase OC condition. Additionally, it also should be noticed that the layout of the remaining windings in the DTP-DS machine is identical to that of the original windings in the Toyota Prius 2010 IPM machine. It is expected that the DTP-DS winding configuration can have a good performance under this condition.

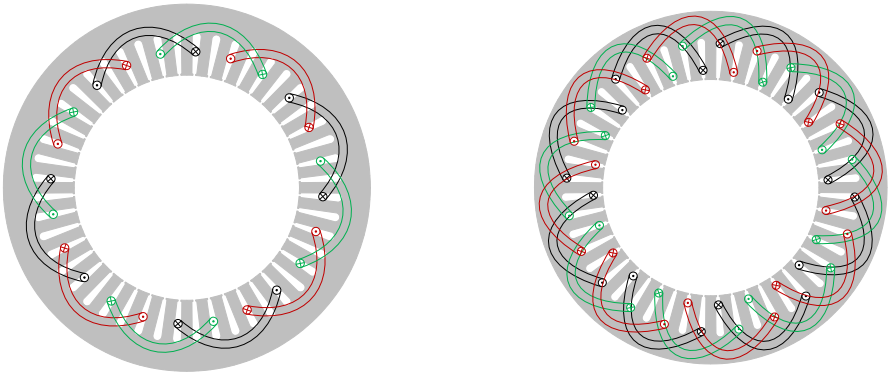

(**a**) (**b**)

Figure 36. Winding layouts of remaining winding set in DTP machines: (**a**) DTP-SF; (**b**) DTP-DS.

4.2. Torque

4.2.1. Instantaneous Torque Waveforms

As discussed before, the instantaneous torque characteristics of the two winding configurations are examined under the maximum torque condition. The phase currents in the remaining windings are 118 Apk, and the current advancing angle is set to produce the highest output torque. The waveforms and spectra of the instantaneous torque under this condition are shown in Figure 37, and the key characteristics are listed in Table 9. From Figure 37 and Table 9, it can be seen that the average output torque of the DTP-DS winding configuration is higher than that of the DTP-SF counterpart, while the torque pulsation of the DTP-DS winding configuration is lower. From Figure 37b, it is observed that the sixth torque harmonics cannot be eliminated in both machines under this condition, and the amplitude of the sixth torque harmonic in the DTP-SF machine is higher than that in the DTP-DS machine. In fact, it is expected that the torque harmonics in the DTP-SF machine are relatively abundant because the winding factors for all harmonic orders are 1 in full-pitched windings. However, the winding factors for the fifth and seventh harmonics are reduced by the short-pitched windings in the DTP-DS winding configuration. Hence, from the viewpoint of the instantaneous torque characteristic, the DTP-DS winding configuration is better under this condition.

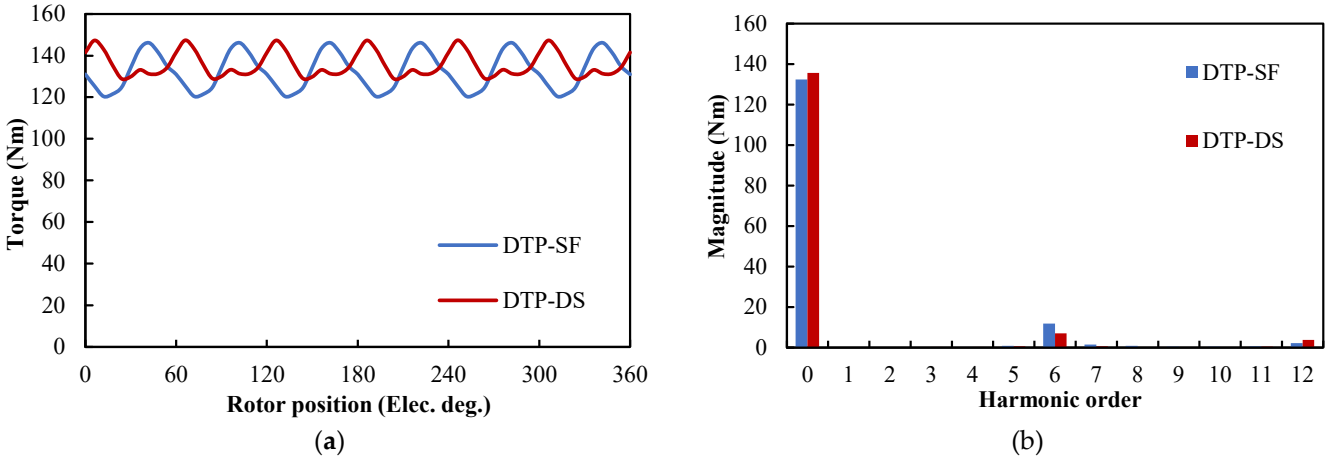

(a) (b)

Figure 37. Instantaneous torque characteristics of different winding configurations under three-phase OC maximum torque condition: (**a**) waveforms; (**b**) spectra.

Table 9. Comparison of instantaneous torque characteristics of different winding configurations under the three-phase OC maximum torque condition.

	DTP-SF	DTP-DS
Average torque (Nm)	132.35	135.56
Torque ripple (Nm)	25.76	18.49
Torque ripple (%)	19.46	13.64

4.2.2. Average Torque and Torque Ripple–Current Amplitude Characteristics

The variations of average torque and torque ripple with phase current amplitude are also considered, as shown in Figure 38. From Figure 38a, it can be seen that when the phase current amplitude is less than 50A, the average torque produced by the two winding configurations is very similar. However, when the phase current amplitude is higher than 75A, the DTP-DS machine can always produce higher average torque than the DTP-SF counterpart. When it comes to torque ripple, it is obvious that the torque ripple in the DTP-DS machine is lower than that in the DTP-SF machine. In Figure 38b, it can be seen that the torque ripple in DTP-SF is decreased with the increase in phase currents. However, even with the 118 Apk phase currents, the torque ripple in the DTP-SF machine is still higher than that in the DTP-DS machine.

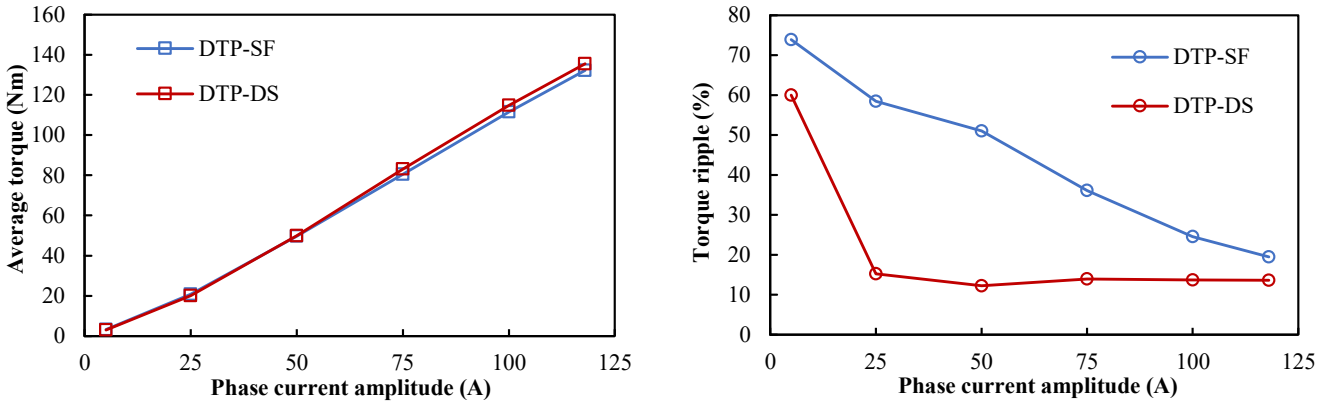

(a) (b)

Figure 38. Torque-current amplitude characteristics of different winding configurations with MTPA strategy under the three-phase OC condition: (**a**) average torque; (**b**) torque ripple.

In [23], it is mentioned that the phase currents in the remaining winding set can be doubled to try to keep the original output torque. In Figure 39, the variations of average

torque and torque ripple with phase current amplitude are examined up to phase current = 250 Apk. From Figure 39a, the average torque produced by the DTP-DS machine is even higher than the DTP-SF machine with high phase currents. In Figure 38b, it seems that the torque ripple in the DTP-SF machine is decreased with the increase in phase current amplitude. However, from Figure 39b, it can be found that the torque ripple in the DTP-SF machine reaches its minimum value around phase current = 150 Apk. Even under this condition, the torque pulsation in the DTP-SF machine is still higher than that in the DTP-DS counterpart. Thus, it can be concluded that the DTP-DS machine always has lower torque pulsation under the three-phase OC condition, no matter what the excitation is.

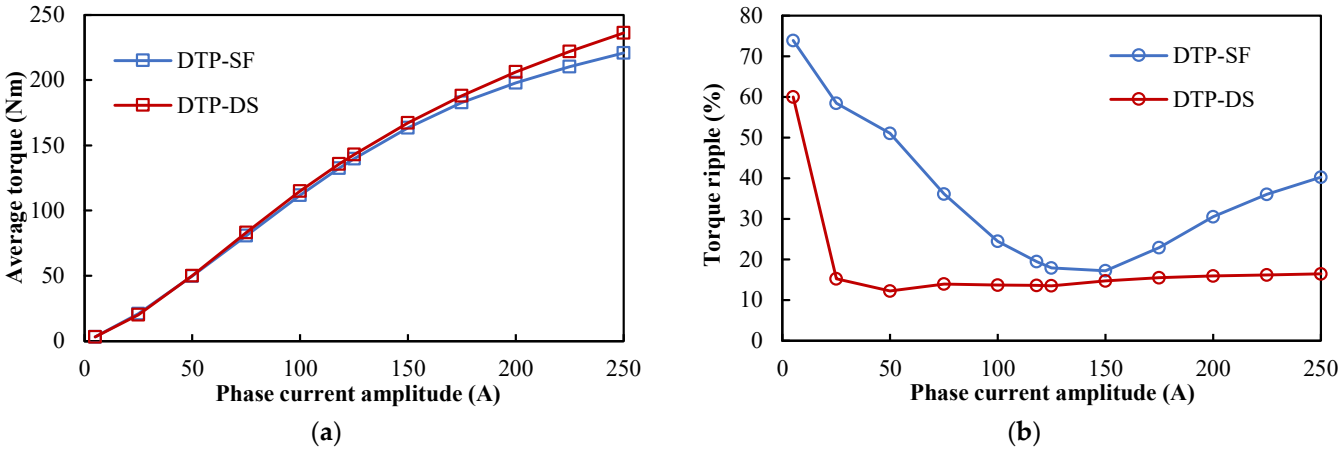

Figure 39. Torque-current amplitude characteristics of different winding configurations with the MTPA strategy under the three-phase OC condition considering over-loading: (**a**) average torque; (**b**) torque ripple.

4.3. Loss and Efficiency

To make an all-around comparison between the DTP-SF and DTP-DS winding configurations, the loss and efficiency performances of them are compared with 118 Apk phase currents, under the three-phase OC condition, as shown in Table 10. Due to the relatively lower output torque, the output power is lower in the DTP-SF machine. In addition, the copper loss in the DTP-SF machine is higher than that in the DTP-DS counterpart because of the longer winding length. What is more, the PM eddy loss can be reduced by DTP-DS windings with lower MMF harmonics. Thus, the overall efficiency of the DTP-DS winding configuration is higher than that of the DTP-SF counterpart by more than 2% under this condition.

Table 10. Loss and efficiency of different winding configurations under three-phase OC maximum torque condition.

	DTP-SF	**DTP-DS**
Speed (rpm)	3000	3000
Average torque (Nm)	132.35	135.56
Copper loss (W)	7283.49	6432.89
Iron loss (W)	245.53	247.14
PM eddy loss (W)	230.49	44.11
Mechanical loss (W)	93.20	93.20
Output power (W)	41578.68	42587.43
Total loss (W)	7852.70	6817.34
Input power (W)	49431.68	49404.77
Efficiency (%)	84.11	86.20

4.4. Summary

Based on the analyses presented in this section, it can be summarized that the DTP-DS winding configuration has better performance under the three-phase OC condition. In general, the DTP-DS machine always has larger average torque and lower torque pulsation than the DTP-SF counterpart. Furthermore, the efficiency of the DTP-DS winding configuration is also higher than that of the DTP-SF counterpart.

5. Experimental Validation

According to the analyses shown in Sections 3 and 4, it can be concluded that both DTP-SF and DTP-DS winding configurations can improve average torque and reduce torque ripple in the Toyota Prius 2010 IPM machine, and the DTP-DS winding configuration has better performance in torque and efficiency under high-speed and three-phase OC conditions. To verify the analyses above, a Toyota Prius 2010 IPM machine equipped with DTP-DS windings is manufactured and tested. The photos of the prototype and the test rig are shown in Figure 40a,b, respectively.

(**a**) (**b**)

Figure 40. Photos of prototype and test rig: (**a**) prototype; (**b**) test rig.

The back EMF performance of the prototype is tested at 1000 rpm. The waveforms and spectra of FE-predicted and tested results are shown in Figure 41. It should be mentioned 3D FE method is also utilized to improve the accuracy of FE simulations. Although the tested back EMF is slightly lower than the FE-predicted values, it still can be found that the tested results agree well with FE-predicted results, and the 3D FE results agree with the experimental results better.

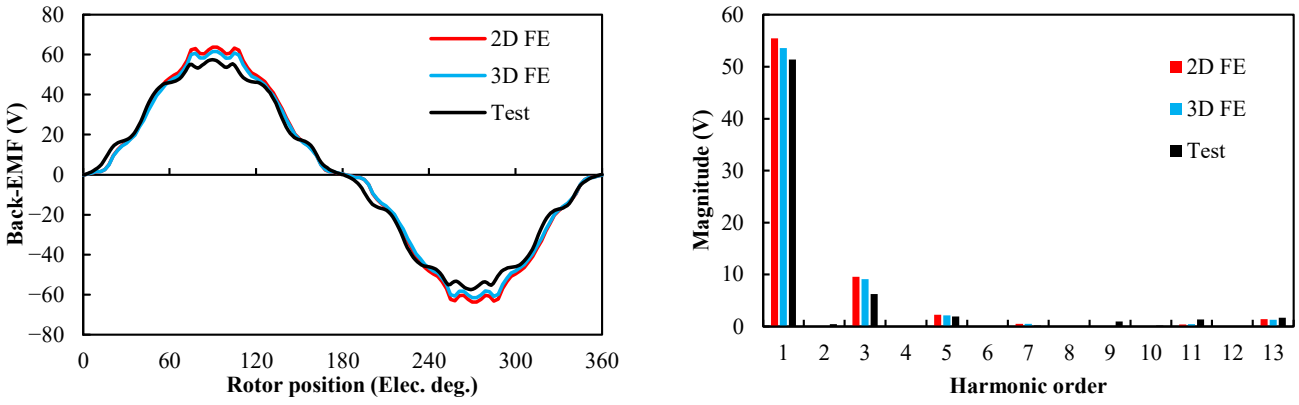

(**a**) (**b**)

Figure 41. Phase back EMF comparison between FE and measured results at 1000 rpm: (**a**) waveforms; (**b**) spectra.

It should be mentioned again that the magnet and core materials used in the FE models are not the actual materials equipped in the prototype. The precision of the FE simulations can be further improved with more accurate material characteristics. However, the agreements between simulated results and tested results shown in Figure 41 are good enough to confirm the correctness of the FE analyses.

The on-load experiment is carried out with 20 Apk phase currents firstly. The on-load torque is measured using a torque transducer with a load machine. Since the torque transducer is connected to the prototype machine and the load machine by shaft couplings, the measured torque is affected by shaft couplings and the load machine. Hence, the measurement of instantaneous torque is very difficult. What is more, the torque pulsations in the prototype machine can be reduced by the load machine and the shaft couplings. The measured torque ripple is lower than the real torque ripple produced by the prototype machine.

The waveforms and spectra of instantaneous torque under this condition are shown in Figure 42 and compared with 2D and 3D FE analysis results. A good agreement between FE-predicted and measured results can be found in Figure 42.

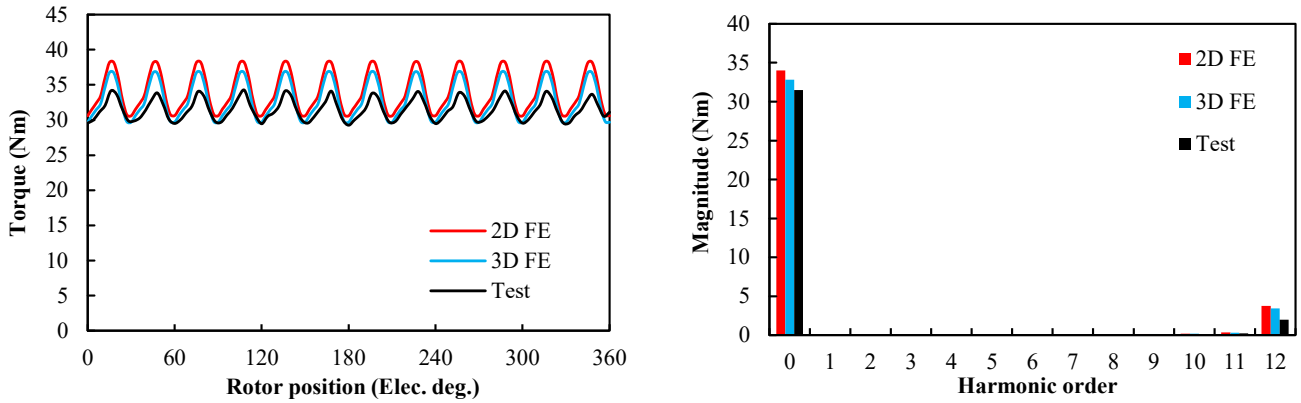

Figure 42. Instantaneous torque comparison between FE and measured results @20 Apk phase currents: (**a**) waveforms; (**b**) spectra.

Then, the torque-current amplitude characteristics of the prototype are also tested. However, it should be mentioned that to simplify the operations, the $I_d = 0$ control strategy is utilized in the experiments instead of the MTPA strategy mentioned in Section 3. The variations of average torque and torque ripple with phase current amplitude are summarized and compared with FE-predicted results in Figure 43. It can be seen that the measured average torque is slightly lower than the calculated results and the measured torque ripples are relatively much lower than simulation results. It was mentioned above that the torque transducer is implemented in the test rig with shaft couplings. The measured torque is not the real output torque of the prototype since the measured torque is filtered by the shaft and the whole test rig. Hence, the measured torque ripples are significantly lower than the calculated results, especially when phase current is high. In general, the FE-predicted average torques still agree well with measured ones, especially the 3D FE-predicted results.

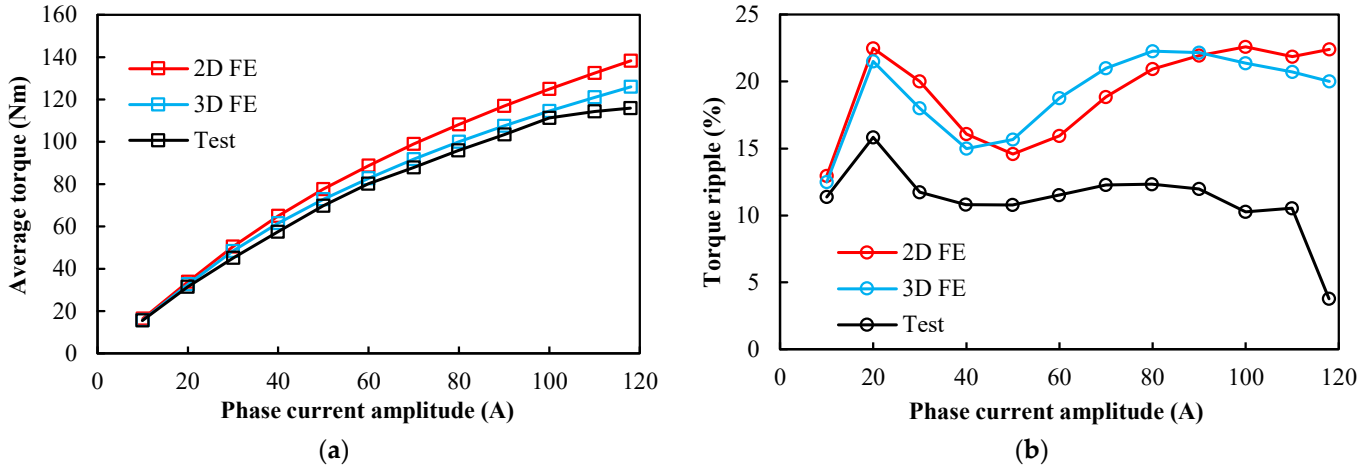

Figure 43. Torque-current amplitude characteristics comparison between FE and measured results with the $I_d = 0$ control strategy: (**a**) Average torque; (**b**) Torque ripple.

6. Conclusions

In this paper, the 48-slot/8-pole Toyota Prius 2010 IPM machine is analyzed, and two DTP winding configurations (DTP-SF and DTP-DS) are introduced to convert it into a DTP machine with a 30° phase shift. The electromagnetic performances of the machine with ORG, DTP-SF, and DTP-DS windings are simulated by the FE method and compared in detail by considering various conditions. Then, a Toyota Prius 2010 IPM machine equipped with DTP-DS windings was manufactured to validate the FE analyses. Some new findings can be obtained from this paper, including:

(1) Only the DTP-SF winding configuration can improve the winding factor of the ORG machine. DTP-DS windings share the same winding factors as ORG windings.
(2) In the constant torque region, DTP-SF windings can produce higher torque than DTP-DS and ORG windings. The output torque of the DTP-DS machine is only slightly higher than that of the ORG machine in this region. Both DTP-SF and DTP-DS winding configurations can reduce torque ripples significantly, and the torque ripple in the DTP-DS machine is even lower.
(3) In the constant power region, the DTP-DS machine has the largest torque output capacity and the lowest torque pulsation. However, the output torque of the DTP-SF machine is lower than that of the ORG machine in this region.
(4) The full-pitched windings utilized in the DTP-SF machine result in the highest copper loss among the three counterparts. Considering that the output torque of the DTP-DS machine is slightly higher than that of the ORG machine, the DTP-DS machine has a better efficiency performance than the ORG machine, and the DTP-SF machine shows the worst efficiency performance.
(5) The electromagnetic performances of DTP-SF and DTP-DS machines under the three-phase OC condition show that DTP-DS machine has better performance in almost all aspects, including average torque, torque ripple, and efficiency.
(6) The stator and rotor cores and magnets of ORG, DTP-SF, and DTP-DS machines are totally identical. The differences in overall costs only lie in the drive system and winding topologies. Compared with the ORG machine, the DTP-SF and DTP-DS machines need another two half-rating inverters and the DTP-DS machine needs more copper wires due to the longer pitched windings.

Overall, the pros and cons of ORG, DTP-SF, and DTP-DS machines are summarized in Table 11.

Table 11. Pros and cons of different winding configurations under maximum torque conditions.

	ORG	DTP-SF	DTP-DS
Pros	• Simple winding connections • Simple drive system	• Highest torque under healthy condition • Lower torque pulsation under healthy condition (Compare with ORG) • Ability to run under three-phase OC condition	• Slightly higher torque under healthy condition (Compare with ORG) • Lower torque pulsation under healthy condition (Compare with ORG) • Slightly higher efficiency (Compare with ORG) • Highest torque under high-speed healthy condition • Ability to run under three-phase OC condition • Higher average torque and lower torque pulsation under three-phase OC condition (Compare with DTP-SF)
Cons	• Lower average torque and higher torque pulsation under healthy condition • Cannot run under three-phase OC condition	• Complex winding connections • Complex drive system • Largest winding usage • Worst efficiency performance • Lowest torque under high-speed healthy condition • Worse torque performance under three-phase OC condition (Compare with DTP-DS)	• Complex winding connections • Complex drive system

Although the DTP-SF winding configuration can increase the winding factor and produce slightly higher torque in the constant torque region, considering the advantages of the DTP-DS winding configuration in average torque, torque ripple, and efficiency, especially under high-speed and three-phase OC conditions, the DTP-DS winding configuration is preferred for the DTP PM machines in EVs.

Author Contributions: Conceptualization, S.W., Z.Z. and A.P.; methodology, S.W., Z.Z. and A.P.; software, S.W.; validation, A.P., J.S. and R.D.; formal analysis, S.W., Z.Z. and A.P.; investigation, S.W., Z.Z., J.S. and A.P.; resources, Z.Z. and C.U.; data curation, S.W. and A.P.; writing—original draft preparation, S.W. and Z.Z.; writing—review and editing, Z.Z.; visualization, S.W.; supervision, Z.Z.; project administration, Z.Z. and A.P.; funding acquisition, Z.Z. and C.U. All authors have read and agreed to the published version of the manuscript.

Funding: This research was funded by IMRA Europe SAS UK Research Centre, under the funding number R/130754-11-1.

Institutional Review Board Statement: Not applicable.

Informed Consent Statement: Not applicable.

Data Availability Statement: Not applicable.

Conflicts of Interest: The authors declare no conflict of interest.

References

1. Zhu, Z.Q.; Howe, D. Electrical machines and drives for electric, hybrid, and fuel cell vehicles. *Proc. IEEE* **2007**, *95*, 746–765. [CrossRef]
2. Zhu, Z.Q.; Chu, W.; Guan, Y. Quantitative comparison of electromagnetic performance of electrical machines for HEVs/EVs. *CES Trans. Electr. Mach. Syst.* **2017**, *1*, 37–47. [CrossRef]

3. Chau, K.T.; Chan, C.C.; Liu, C. Overview of permanent-magnet brushless drives for electric and hybrid electric vehicles. *IEEE Trans. Ind. Electron.* **2008**, *55*, 2246–2257. [CrossRef]
4. Santiago, J.; Bernhoff, H.; Ekergård, B.; Eriksson, S.; Ferhatovic, S.; Waters, R.; Leijon, M. Electrical motor drivelines in commercial all-electric vehicles: A review. *IEEE Trans. Veh. Technol.* **2012**, *61*, 475–484. [CrossRef]
5. Yang, Y.; Castano, S.; Yang, R.; Kasprzak, M.; Bilgin, B.; Sathyan, A.; Dadkhah, H.; Emadi, A. Design and comparison of interior permanent magnet motor topologies for traction applications. *IEEE Trans. Transp. Electrif.* **2017**, *3*, 86–97. [CrossRef]
6. Barcaro, M.; Bianchi, N.; Magnussen, F. Analysis and tests of a dual three-phase 12-slot 10-pole permanent-magnet motor. *IEEE Trans. Ind. Appl.* **2010**, *46*, 2355–2362. [CrossRef]
7. Barcaro, M.; Bianchi, N.; Magnussen, F. Six-phase supply feasibility using a PM fractional-slot dual winding machine. *IEEE Trans. Ind. Appl.* **2011**, *47*, 2042–2050. [CrossRef]
8. Barcaro, M.; Bianchi, N.; Magnussen, F. Faulty operations of a PM fractional-slot machine with a dual three-phase winding. *IEEE Trans. Ind. Electron.* **2010**, *58*, 3825–3832. [CrossRef]
9. Abdel-Khalik, A.S.; Ahmed, S.; Massoud, A.M. Low space harmonics cancelation in double-layer fractional slot winding using dual multiphase winding. *IEEE Trans. Magn.* **2015**, *51*, 8104710. [CrossRef]
10. Abdel-Khalik, A.S.; Ahmed, S.; Massoud, A.M. A six-phase 24-slot/10-pole permanent-magnet machine with low space harmonics for electric vehicle applications. *IEEE Trans. Magn.* **2016**, *52*, 8700110. [CrossRef]
11. Abdel-Khalik, A.S.; Ahmed, S.; Massoud, A.M. Effect of multilayer windings with different stator winding connections on interior PM machines for EV applications. *IEEE Trans. Magn.* **2016**, *52*, 8100807. [CrossRef]
12. Patel, V.I.; Wang, J.; Wang, W.; Chen, X. Six-phase fractional-slot-per-pole-per-phase permanent-magnet machines with low space harmonics for electric vehicle application. *IEEE Trans. Ind. Appl.* **2014**, *50*, 2554–2563. [CrossRef]
13. Patel, V.I.; Wang, J.; Nair, S.S. Demagnetization assessment of fractional-slot and distributed wound 6-phase permanent magnet machines. *IEEE Trans. Magn.* **2015**, *51*, 8105511. [CrossRef]
14. Chen, X.; Wang, J.; Patel, V.I. A generic approach to reduction of magnetomotive force harmonics in permanent-magnet machines with concentrated multiple three-phase windings. *IEEE Trans. Magn.* **2014**, *50*, 8103604. [CrossRef]
15. Chen, X.; Wang, J.; Patel, V.I.; Lazari, P. A nine-phase 18-slot 14-pole interior permanent-magnet machine with low space harmonics for electric vehicle applications. *IEEE Trans. Energy Convers.* **2016**, *31*, 860–871. [CrossRef]
16. Onsal, M.; Demir, Y.; Aydin, M. A new nine-phase permanent magnet synchronous motor with consequent pole rotor for high-power traction applications. *IEEE Trans. Magn.* **2017**, *53*, 8700606. [CrossRef]
17. Zheng, P.; Wu, F.; Sui, Y.; Wang, P.; Lei, Y.; Wang, H. Harmonic analysis and fault-tolerant capability of a semi-12-phase permanent-magnet synchronous machine used for EVs. *Energies* **2012**, *5*, 3586–3607. [CrossRef]
18. Zheng, P.; Wu, F.; Lei, Y.; Sui, Y.; Yu, B. Investigation of a novel 24-slot/14-pole six-phase fault-tolerant modular permanent-magnet in-wheel motor for electric vehicles. *Energies* **2013**, *6*, 4980–5002. [CrossRef]
19. Tong, C.; Wu, F.; Zheng, P.; Sui, Y.; Cheng, L. Analysis and design of a fault-tolerant six-phase permanent-magnet synchronous machine for electric vehicles. In Proceedings of the 17th International Conference on Electrical Machines and Systems (ICEMS), Hangzhou, China, 22–25 October 2014; pp. 1629–1632.
20. Cheng, L.; Sui, Y.; Zheng, P.; Yin, Z.; Wang, C. Investigation of low space harmonic six-phase PMSM with FSCWs for electric vehicle applications. In Proceedings of the IEEE Transportation Electrification Conference and Expo, Asia-Pacific (ITEC Asia-Pacific), Harbin, China, 7–10 August 2017; pp. 1–5.
21. Cheng, L.; Sui, Y.; Zheng, P.; Yin, Z.; Wang, C. Influence of stator MMF harmonics on the utilization of reluctance torque in six-phase PMA-SynRM with FSCW. *Energies* **2018**, *11*, 108. [CrossRef]
22. Zhu, S.; Cox, T.; Xu, Z.; Gerada, C. A novel 24-slots14-poles fractional-slot concentrated winding topology with low space harmonics for electrical machine. In Proceedings of the Power Electronics, Machines and Drives Conference (PEMD), Liverpool, UK, 17–19 April 2018.
23. Xu, P.L.; Feng, J.; Guo, S.; Feng, S.; Chu, W.Q.; Ren, Y.; Zhu, Z.Q. Analysis of dual three-phase permanent magnet synchronous machines with different angle displacements. *IEEE Trans. Ind. Electron.* **2018**, *65*, 1941–1954. [CrossRef]
24. Xu, P.L.; Zhu, Z.Q.; Shao, B.; Wang, S.S.; Feng, J.H.; Guo, S.Y.; Li, Y.F.; Feng, S.Z. Analysis of dual 3-phase fractional-slot non-overlapping winding pm synchronous machines with different angle displacements. In Proceedings of the IEEE Energy Conversion Congress and Exposition (ECCE), Baltimore, MD, USA, 29 September–3 October 2019; pp. 5616–5623.
25. Demir, Y.; Aydin, M. A novel dual three-phase permanent magnet synchronous motor with asymmetric stator winding. *IEEE Trans. Magn.* **2016**, *52*, 8105005. [CrossRef]
26. Demir, Y.; Aydin, M. A novel asymmetric and unconventional stator winding configuration and placement for a dual three-phase surface PM motor. *IEEE Trans. Magn.* **2017**, *53*, 8111805. [CrossRef]
27. Demir, Y.; Aydin, M. Design, analysis and validation of a dual three-phase 72-slot, 12-pole permanent magnet synchronous motor. In Proceedings of the XXII International Conference on Electrical Machines (ICEM), Lausanne, Switzerland, 4–7 September 2016; pp. 1598–1603.
28. Li, Y.X.; Zhu, Z.Q.; Thomas, A.; Wu, Y.; Wu, X.M. Comparison of modular dual 3-phase PM machines with overlapping/non-overlapping windings. *IEEE Trans. Ind. Appl.* **2019**, *55*, 3566–3576. [CrossRef]
29. Li, Y.X.; Zhu, Z.Q.; Thomas, A.S.; Wu, Z.Y.; Wu, X.M. Novel modular fractional slot permanent magnet machines with redundant teeth. *IEEE Trans. Magn.* **2019**, *55*, 8204810. [CrossRef]

30. Li, Y.X.; Zhu, Z.Q.; Thomas, A.S. Generic slot and pole number combinations for novel modular permanent magnet dual 3-phase machines with redundant teeth. *IEEE Trans. Energy Convers.* **2020**, *35*, 1676–1687. [CrossRef]
31. Miyama, Y.; Akatsu, K. Technical arrangement of high-performance techniques achieved by multi-phase permanent magnet synchronous motor systems. In Proceedings of the IEEE Energy Conversion Congress and Exposition (ECCE), Portland, OR, USA, 23–27 September 2018; pp. 1574–1580.
32. Miyama, Y.; Ishizuka, M.; Kometani, H.; Akatsu, K. Vibration reduction by applying carrier phase-shift PWM on dual three-phase winding permanent magnet synchronous motor. *IEEE Trans. Ind. Appl.* **2018**, *54*, 5998–6004. [CrossRef]
33. Zhang, W.; Xu, Y.; Huang, H.; Zou, J. Vibration reduction for dual-branch three-phase permanent magnet synchronous motor with carrier phase-shift technique. *IEEE Trans. Power Electron.* **2020**, *35*, 607–618. [CrossRef]
34. Wang, X.; Sala, G.; Buticchi, G.; Gu, C.; Zhao, W.; Xu, L.; Zhang, H. Selective torque harmonic elimination for dual three-phase pmsms based on PWM carrier phase shift. *IEEE Trans. Power Electron.* **2020**, *35*, 13255–13269. [CrossRef]
35. Zhu, Z.; Wang, S.; Shao, B.; Yan, L.; Xu, P.; Ren, Y. Advances in dual-three-phase permanent magnet synchronous machines and control techniques. *Energies* **2021**, *14*, 7508. [CrossRef]
36. Yang, R.; Schofield, N.; Zhao, N.; Emadi, A. Dual three-phase permanent magnet synchronous machine investigation for battery electric vehicle power-trains. *J. Eng.* **2019**, *17*, 3981–3985. [CrossRef]
37. Döbler, R.; Schuhmann, T.; Inderka, R.B.; Malottki, S.V. High performance drive for electric vehicles—System comparison between three and six phase permanent magnet synchronous machines. In Proceedings of the 18th European Conference on Power Electronics and Applications (EPE'16 ECCE Europe), Karlsruhe, Germany, 5–9 September 2016; pp. 1–10.
38. Keller, D.; Karayel, A.; Parspour, N. Comparison of two different winding sets for dual three-phase permanent magnet machines. In Proceedings of the 9th International Electric Drives Production Conference (EDPC), Esslingen, Germany, 3–4 December 2019; pp. 1–6.
39. Taniguchi, M.; Yashiro, T.; Takizawa, K.; Baba, S.; Tsuchida, M.; Mizutani, T.; Endo, H.; Kimura, H. Development of New Hybrid Transaxle for Compact-Class Vehicles. *SAE Tech. Pap.* **2016**. [CrossRef]
40. Hsu, J.S. *Report on Toyota/Prius Motor Torque-Capability, Torque-Property, No-Load Back EMF, and Mechanical Losses*; Department of Energy: Oak Ridge, TN, USA, 2004.
41. Burress, T.A.; Campbell, S.L.; Coomer, C.; Seiber, L.E.; Marino, L.D.; Wereszczak, A.A.; Lin, H.T.; Ayers, C.W. *Evaluation of the 2010 Toyota PRIUS Hybrid Synergy Drive System*; Oak Ridge National Laboratory (ORNL): Oak Ridge, TN, USA, 2011.
42. JMAG User Support. Available online: https://www.jmag-international.com/supports/ (accessed on 6 February 2022).
43. Infineon Design Support. Available online: https://www.infineon.com/cms/en/design-support/ (accessed on 6 February 2022).
44. Wang, S.; Zhu, Z.Q.; Pride, A.; Deodhar, R.; Umemura, C. Torque separation for dual three-phase pm machines using frozen permeability method. In Proceedings of the International Conference on Power Electronics, Machines and Drives (PEMD), Online, 15–17 December 2020; pp. 204–209.
45. Qi, G.; Chen, J.T.; Zhu, Z.Q.; Howe, D.; Zhou, L.B.; Gu, C.L. Influence of skew and cross-coupling on flux-weakening performance of permanent-magnet brushless AC machines. *IEEE Trans. Magn.* **2009**, *45*, 2110–2117. [CrossRef]